



Natural Resources
Canada

Ressources naturelles
Canada

**GEOLOGICAL SURVEY OF CANADA
OPEN FILE 8007**

**Modelling the magnetic field of the solar corona with
potential-field source-surface and Schatten current sheet
models**

L. Nikolic

2017



Canada 



GEOLOGICAL SURVEY OF CANADA OPEN FILE 8007

Modelling the magnetic field of the solar corona with potential-field source-surface and Schatten current sheet models

L. Nikolic

2017

© Her Majesty the Queen in Right of Canada, as represented by the Minister of Natural Resources, 2017

Information contained in this publication or product may be reproduced, in part or in whole, and by any means, for personal or public non-commercial purposes, without charge or further permission, unless otherwise specified.

You are asked to:

- exercise due diligence in ensuring the accuracy of the materials reproduced;
- indicate the complete title of the materials reproduced, and the name of the author organization; and
- indicate that the reproduction is a copy of an official work that is published by Natural Resources Canada (NRCan) and that the reproduction has not been produced in affiliation with, or with the endorsement of, NRCan.

Commercial reproduction and distribution is prohibited except with written permission from NRCan. For more information, contact NRCan at nrcan.copyrightdroitdauteur.nrcan@canada.ca.

doi:10.4095/300826

This publication is available for free download through GEOSCAN (<http://geoscan.nrcan.gc.ca/>).

Recommended citation

Nikolic, L., 2017. Modelling the magnetic field of the solar corona with potential-field source-surface and Schatten current sheet models; Geological Survey of Canada, Open File 8007, 69 p. doi:10.4095/300826

Modelling the magnetic field of the solar corona with potential-field source-surface and Schatten current sheet models

Ljubomir Nikolić

Contents

1	Introduction	4
2	Potential-field source-surface (PFSS) model	7
2.1	Current-free approximation of the coronal magnetic field	7
2.2	Laplace equation - radial solution	8
2.3	Laplace equation - angular solution	8
2.4	Coronal magnetic field between the Sun and the source-surface	11
3	Schatten current sheet (SCS) model	14
3.1	Coronal magnetic field beyond the source-surface	14
4	Numerical solutions with GONG magnetograms	18
4.1	Number of spherical harmonics	18
4.2	Re-meshed magnetograms	27
4.3	Angular resolution	37
4.4	Schatten model - principal index N_s	44
4.5	Radial resolution	49
4.6	Height of the source-surface	52
5	Summary	65
	Acknowledgment	67
	References	68

1 Introduction

Space weather can have adverse effects on modern technology and human activities and is recognized as a natural hazard of the technological age. The need to understand and mitigate effects of space weather phenomena has stimulated research activities targeted toward operational space weather forecasting. A number of forecast centres have been established to provide information on global and regional space weather conditions [1]. In Canada, Natural Resources Canada has undertaken space weather activities on both, the research side through the Public Safety Geoscience Program, and the operational side through the Canadian Hazards Information Service which operates the Canadian Space Weather Forecast Centre (CSWFC) [2].

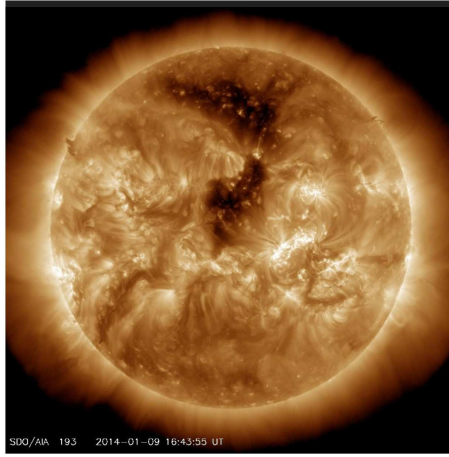


Figure 1: SDO satellite AIA-193 image of the Sun on 09 January 2014. The dark regions on the solar disc represent coronal holes while bright features represent active regions and coronal loops.

Forecasting space weather is a challenging task. There are still many unanswered questions concerning space weather. More research is needed to understand space weather processes including solar activity which is the driver of space weather. Ground and satellite observations of the Sun’s surface and solar atmosphere are a crucial tool that provides the space weather research and forecasting communities with information about the generation and dynamics of solar disturbances. An example of solar observations is shown in Fig. 1. The figure shows an extreme ultraviolet (EUV) image of the solar corona taken by the Solar Dynamics Observatory (SDO) satellite on 09 January 2014 [3]. The bright features in the image represent active regions and magnetic field loops where coronal plasma is strongly confined. In contrast, the dark areas on the solar disc, called coronal holes (COHO), are associated with plasma which freely escapes the lower corona along open magnetic field lines. It is widely accepted that high speed ($\sim 500 - 800$ km/s) solar wind streams (HSS) emanate from COHO. The origin of slow solar wind ($\sim 300 - 400$ km/s) is still not well understood [4].

The configuration and evolution of the Sun’s magnetic field is a key component that triggers and influences solar outputs such as solar wind, solar flares and coronal mass ejections (CME). Sunspots, which represent “islands” of very strong photospheric magnetic

field are an indicator of magnetic field evolution. Changes in the number of the sunspots follow an approximately 11 year cycle, giving rise to quiet and active periods of solar activity. To illustrate this, in Fig. 2 the solar radio flux at a 10.7cm wavelength ($F_{10.7}$) for 1947-2014 (Fig. 2a, monthly averaged), and 2007-2014 (Fig. 2b, daily measured) is shown. The radio flux is measured by the Dominion Radio Astrophysical Observatory (DRAO, National Research Council Canada) [5]. The flux plotted in Fig. 2 is expressed in solar flux units ($1 \text{ sfu} = 10^{-22} \text{ W m}^{-2} \text{ Hz}^{-1}$), and represents so called adjusted flux, i.e. the flux corrected for variations in the Sun-Earth distance. $F_{10.7}$ depends on the intensity of the solar magnetic field and is correlated with the sunspot number.

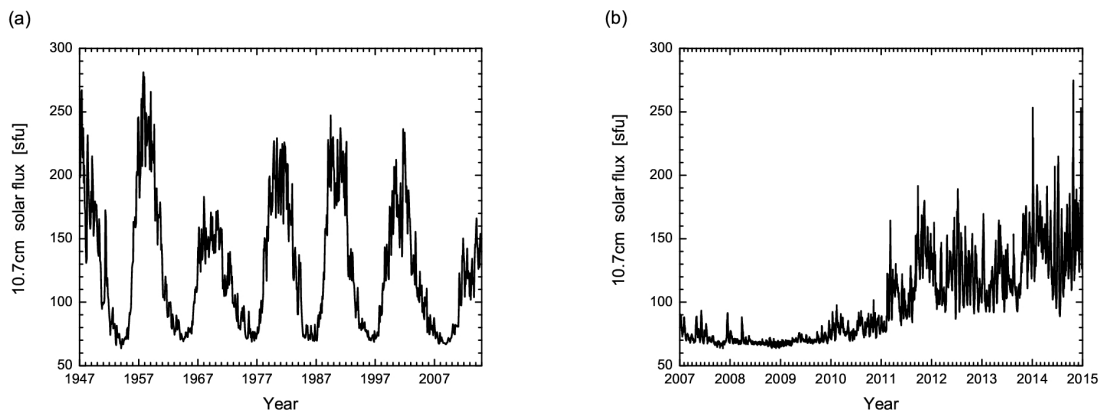


Figure 2: Adjusted 10.7cm solar radio flux. (a) Monthly averaged for 1947-2014 and (b) daily measured for 2007-2014.

During quiet years, which fall around the minima of the $F_{10.7}$ curve shown in Fig. 2a, the coronal magnetic field resembles a dipole with open magnetic field lines rooted mainly in the polar regions of the Sun. The consequence of this field configuration is the formation of large polar COHO. During a low solar activity period, space weather effects associated with HSS from high-latitude COHO prevail. As the solar cycle progresses, more sunspots start to appear on the solar disc and the magnetic structure of the corona becomes more complex (see Fig. 1). This higher solar activity period of the solar cycle is characterized by an increased number of solar flares and CMEs which can be followed by solar energetic particle events. Moreover, during this period low-latitude, usually smaller, COHO emerge.

Reconstruction and quantification of the coronal magnetic field from solar observations poses a challenge. The direct measurements of the field, using the Zeeman spectral line splitting effect, are mainly limited to photospheric - chromospheric heights ($< 2500 \text{ km}$). An example of the magnetic field measurement is shown in Fig. 3 for Carrington rotations (CR) 2077 (Fig. 3a) and 2147 (Fig. 3b). These magnetograms are obtained by the Global Oscillation Network Group (GONG) [6], and represent full-surface maps of the magnetic field radial component at the photosphere $B_r(R_0)$. The field in Fig. 3 is saturated at $\pm 15 \text{ G}$. The red and blue colours represent $B_r(R_0)$ which is directed away from and toward the surface of the Sun, respectively. As we can see from Fig. 2b, CR2017 and CR2147 magnetograms capture solar minimum (CR2077) and maximum (CR2147).

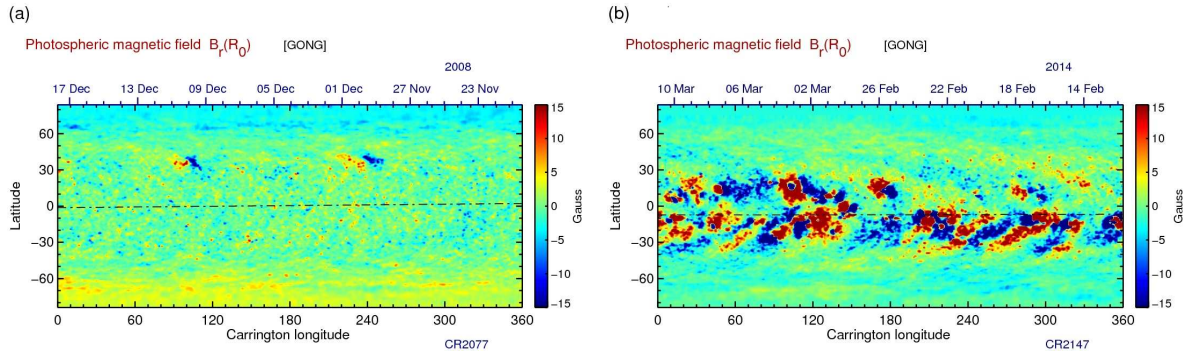


Figure 3: Full-surface GONG magnetograms for (a) CR2077 and (b) CR2147. The magnetograms represent the photospheric radial component $B_r(R_0)$ of the magnetic field. The field scale is saturated at ± 15 G. Dash-dot line represents the sub-Earth positions.

To derive a global coronal magnetic field and to infer properties of the corona using solar magnetograms as an input, numerical models based on different approximations are used [7]. Since the coupling between charged particles and fields is described self-consistently, the Magnetohydrodynamics (MHD) models would be one of the best ways to treat the problem. However, they also require assumptions and boundary conditions, such as plasma temperature and density, which are difficult to derive from solar observations. Therefore, the MHD solutions for the global steady-state magnetic structure of the corona do not always offer significant advantage over solutions obtained by more restrictive approximations, such as force-free or potential-field models [8]. Although the potential-field models, proposed in 1969 [9], [10], represent a simple approach where the plasma dynamics are neglected, they are still a widely used numerical tool to investigate and reproduce observed coronal features. The potential-field models are computationally not too demanding and their inputs, i.e. magnetograms, are regularly available.

A numerical code for the global coronal magnetic field, based on potential-field source-surface (PFSS) and Schatten current sheet (SCS) models [9]-[12], has been developed at the CSWFC. The reason for the development lies in the fact that these models are used not only in the research community but in operational applications as well. For example, these models are used as a base for solar wind speed and magnetic field polarity forecasts [13]-[17], to provide initial conditions to MHD space weather codes [18]-[20], etc. We plan to use the developed code as part of CSWFC solar wind forecast framework.

The purpose of this paper is to describe the theoretical approach and numerical methods used in the CSWFC PFSS - SCS code. In Section 2 the PFSS model equations are derived, and in Section 3 an extension of the magnetic field beyond the “source-surface” proposed by Schatten [12] is presented. In Section 4, a brief description of numerical techniques and investigation of the dependence of the code outputs on numerical parameters are given. The numerical results are obtained using GONG magnetograms, in particular by those shown in Fig. 3. The summary is given in Section 5.

2 Potential-field source-surface (PFSS) model

The motion of charged particles in the corona is coupled with the magnetic field generated by the solar dynamo. In the lower corona, where the magnetic field is strong, the magnetic field pressure p_B dominates over the plasma thermal pressure p_{th} [21], i.e.

$$\beta = \frac{p_{th}}{p_B} = \frac{nk_bT}{B^2/(2\mu_0)} \ll 1, \quad (1)$$

where n is the particle density, k_b is Boltzmann's constant, T is the temperature, B is the magnetic field intensity and μ_0 is the magnetic permeability of a vacuum. In other words, in the region where $\beta \ll 1$, the structure of the Sun's atmosphere and the plasma dynamics are defined by the Sun's magnetic field. Moving outward from the lower corona, due to coronal heating of the plasma and lower magnetic field intensity, plasma motion starts to play a key role. The plasma currents distort the magnetic field lines and, in the $\beta > 1$ region where the plasma thermal pressure dominates, the magnetic field lines are carried along by the highly conductive solar wind outflow.

In the following we will focus our attention on the coronal region where plasma β is less than unity. Assuming a stationary state, the magnetic field properties are given by (see e.g. [22]):

$$\nabla \cdot \mathbf{B} = 0, \quad (2)$$

$$\nabla \times \mathbf{B} = \mu_0 \mathbf{j}, \quad (3)$$

where \mathbf{j} is the electric current. Neglecting the Lorentz force

$$\mathbf{F} = \mathbf{j} \times \mathbf{B} = 0, \quad (4)$$

in combination with Eq. (3) gives

$$(\nabla \times \mathbf{B}) \times \mathbf{B} = 0, \quad (5)$$

which is satisfied if

$$\mathbf{B} \parallel (\nabla \times \mathbf{B}), \quad \text{or} \quad (6)$$

$$\nabla \times \mathbf{B} = 0. \quad (7)$$

The condition expressed by Eq. (6) leads to so-called force-free models where currents are allowed to flow along the magnetic field lines, while Eq. (7) represents the current-free approximation.

2.1 Current-free approximation of the coronal magnetic field

The current-free approximation Eq. (7) implies that the magnetic field can be expressed as the gradient of a scalar potential Ψ ,

$$\mathbf{B} = -\nabla \Psi. \quad (8)$$

Taking into account the divergenceless property of the magnetic field Eq. (2), this potential-field equation gives the Laplace equation for the scalar potential

$$\nabla^2 \Psi = 0. \quad (9)$$

Using the separation of variables $\Psi(r, \theta, \phi) = \Lambda(r)\Theta(\theta)\Phi(\phi)$ in spherical coordinates (r, θ, ϕ) , where r is the radius, θ is the colatitude ($\theta \in [0, \pi]$), and ϕ is the longitude ($\phi \in [0, 2\pi]$), the Laplace equation (9) can be rewritten as:

$$\frac{r^2}{\Psi} \nabla^2 \Psi = \frac{1}{\Lambda} \frac{d}{dr} \left(r^2 \frac{d\Lambda}{dr} \right) + \frac{1}{\Theta \sin \theta} \frac{d}{d\theta} \left(\sin \theta \frac{d\Theta}{d\theta} \right) + \frac{1}{\Phi \sin^2 \theta} \frac{d^2 \Phi}{d\phi^2} = 0. \quad (10)$$

Since expressions for the radial r and angular (θ, ϕ) part in Eq. (10) are independent, they must be constant. Writing the separation constant as $n(n+1)$, we obtain

$$\frac{1}{\Lambda} \frac{d}{dr} \left(r^2 \frac{d\Lambda}{dr} \right) = n(n+1), \quad (11)$$

for the radial part and

$$\frac{1}{\Theta \sin \theta} \frac{d}{d\theta} \left(\sin \theta \frac{d\Theta}{d\theta} \right) + \frac{1}{\Phi \sin^2 \theta} \frac{d^2 \Phi}{d\phi^2} = -n(n+1), \quad (12)$$

for the angular part of the Laplace equation.

2.2 Laplace equation - radial solution

Equation (11) represents an Euler differential equation,

$$\frac{r^2}{\Lambda} \frac{d^2 \Lambda}{dr^2} + \frac{2r}{\Lambda} \frac{d\Lambda}{dr} = n(n+1), \quad (13)$$

which can be solved by looking for solutions of the form $\Lambda(r) \propto r^k$. Inserting the proposed solution into Eq. (13) we obtain

$$[k(k+1) - n(n+1)] r^k = 0, \quad (14)$$

which is satisfied if $k = n$ or $k = -(n+1)$. Therefore, the radial solution $\Lambda(r)$ of the Laplace equation (11) is $a_n r^n$ or $b_n r^{-(n+1)}$, or their linear combination

$$\Lambda_n(r) = a_n r^n + b_n \frac{1}{r^{n+1}}, \quad (15)$$

where a_n and b_n are constants.

2.3 Laplace equation - angular solution

The angular part Eq. (12) of the Laplace equation can also be separated into ϕ and θ components. Taking the separation constant as m^2 , from Eq. (12) we get

$$\frac{1}{\Phi} \frac{d^2 \Phi}{d\phi^2} + m^2 = 0, \quad (16)$$

and

$$\frac{\sin \theta}{\Theta} \frac{d}{d\theta} \left(\sin \theta \frac{d\Theta}{d\theta} \right) + n(n+1) \sin^2 \theta - m^2 = 0. \quad (17)$$

The solution of Eq. (16) is $\Phi \propto e^{im\phi}$. Since the function Φ should satisfy longitudinal periodicity $\Phi(\phi) = \Phi(\phi + 2\pi)$ and $\Phi'(\phi) = \Phi'(\phi + 2\pi)$, the constant m must be an integer. Thus, the general solution of Eq. (16) is

$$\Phi_m(\phi) = c_m \cos m\phi + d_m \sin m\phi \quad \text{with } m = 0, 1, 2, \dots \quad (18)$$

where c_m and d_m are constants.

To solve part of the Laplace equation which depends on the colatitude θ , we introduce the substitution $\mu = \cos \theta$ in Eq. (17). Thus, we have

$$\frac{d}{d\mu} \left[(1 - \mu^2) \frac{d\Theta}{d\mu} \right] + \left[n(n+1) - \frac{m^2}{1 - \mu^2} \right] \Theta = 0. \quad (19)$$

This equation represents the associated Legendre differential equation of order m . It is clear now why we wrote the separation constant between the radial and angular part in Eq. (11) and (12) as $n(n+1)$.

Since $-1 \leq \mu \leq 1$ ($\theta \in [0, \pi]$), the associated Legendre differential equation (19) has regular singular points for $\mu = \pm 1$. It can be shown that the solution $\Theta(\mu)$ is finite at the poles if $n = 0, 1, 2, \dots$ (see e.g. [23] p.246). For $m = 0$ the solutions $\Theta(\mu)$ of Eq. (19) are called Legendre polynomials $P_n(\mu)$,

$$P_n(\mu) = \frac{1}{2^n n!} \frac{d^n}{d\mu^n} (\mu^2 - 1)^n, \quad (20)$$

and for $m \neq 0$ the solutions are associated Legendre polynomials $P_{n,m}(\mu)$ (see e.g. [24] p.609, [25]),

$$P_{n,m}(\mu) = (1 - \mu^2)^{\frac{m}{2}} \frac{d^m P_n(\mu)}{d\mu^m}, \quad (21)$$

where n and m denote the degree and order of the polynomial, respectively. Note that $P_{n,0}(\mu) = P_n(\mu)$. Furthermore, from Eq. (20) and (21) it follows

$$P_{n,m}(\mu) = (1 - \mu^2)^{\frac{m}{2}} \frac{1}{2^n n!} \frac{d^{n+m}}{d\mu^{n+m}} (\mu^2 - 1)^n, \quad (22)$$

which gives

$$P_{n,m}(\mu) = 0 \quad \text{for } m > n, \quad (23)$$

$$P_{m,m}(\mu) = (1 - \mu^2)^{\frac{m}{2}} \frac{(2m)!}{2^m m!} \quad \text{for } n = m, \quad (24)$$

and

$$P_{m+1,m}(\mu) = (2m+1)\mu P_{m,m}(\mu) \quad \text{for } n = m+1. \quad (25)$$

It can be shown that the following recursion relation also holds

$$P_{n,m}(\mu) = \frac{2n-1}{n-m} \mu P_{n-1,m}(\mu) - \frac{n-1+m}{n-m} P_{n-2,m}(\mu) \quad \text{for } n \geq m+2. \quad (26)$$

Taking into account Eq. (18) and (21), we see that the solution for the angular part Eq. (12) of the Laplace equation can be represented as a linear combination of spherical harmonics $P_{n,m}(\cos \theta) \cos m\phi$ ($m = 0, 1, \dots, n$) and $P_{n,m}(\cos \theta) \sin m\phi$ ($m = 1, 2, \dots, n$). On the spherical surface, the spherical harmonics are orthogonal. They satisfy

$$\begin{aligned} & \frac{1}{4\pi} \int_0^\pi \int_0^{2\pi} P_{n,m}(\cos \theta) \begin{Bmatrix} \cos m\phi \\ \sin m\phi \end{Bmatrix} P_{n',m'}(\cos \theta) \begin{Bmatrix} \cos m'\phi \\ \sin m'\phi \end{Bmatrix} \sin \theta d\theta d\phi \\ &= \delta_n^{n'} \delta_m^{m'} \frac{1}{2(2n+1)} \frac{(n+m)!}{(n-m)!} \quad \text{for } 0 < m \leq n, \end{aligned} \quad (27)$$

and

$$\begin{aligned} & \frac{1}{4\pi} \int_0^\pi \int_0^{2\pi} P_{n,m}(\cos \theta) \cos m\phi P_{n',m'}(\cos \theta) \cos m'\phi \sin \theta d\theta d\phi \\ &= \delta_n^{n'} \delta_m^{m'} \frac{1}{2n+1} \quad \text{for } m = 0, \end{aligned} \quad (28)$$

where $\delta_n^{n'}$ and $\delta_m^{m'}$ are the Kronecker deltas ($0 < m' \leq n'$, $n' = 0, 1, 2, \dots$). Note also that for $m, m' \geq 0$ we have

$$\frac{1}{4\pi} \int_0^\pi \int_0^{2\pi} P_{n,m}(\cos \theta) \sin m\phi P_{n',m'}(\cos \theta) \cos m'\phi \sin \theta d\theta d\phi = 0. \quad (29)$$

Instead of $P_{n,m}(\cos \theta)$, orthogonal functions $\tilde{P}_n^m(\theta)$ with different normalization factors $k_{n,m}$ are used in different fields of physics,

$$\frac{1}{4\pi} \int_0^\pi \int_0^{2\pi} \tilde{P}_n^m(\theta) \begin{Bmatrix} \cos m\phi \\ \sin m\phi \end{Bmatrix} \tilde{P}_{n'}^{m'}(\theta) \begin{Bmatrix} \cos m'\phi \\ \sin m'\phi \end{Bmatrix} \sin \theta d\theta d\phi = k_{n,m}^2 \delta_n^{n'} \delta_m^{m'}. \quad (30)$$

For $k_{n,m}^2 = 1$, denoting $\tilde{P}_n^m(\theta)$ as $R_n^m(\theta)$ here, from Eq. (30), (27) and (28) we obtain

$$R_n^m(\theta) = \left(\frac{(2 - \delta_m^0)(2n+1)(n-m)!}{(n+m)!} \right)^{\frac{1}{2}} P_{n,m}(\cos \theta). \quad (31)$$

The functions $R_n^m(\theta)$ are completely normalized and are used, for example, in [11] to map the coronal magnetic field. It is useful to derive here some properties of functions $R_n^m(\theta)$ which will allow their numerical generation [11]. From Eq. (31) and (24) for $n = m$ it follows

$$R_m^m(\theta) = \frac{((2 - \delta_m^0)(2m+1)(2m)!)^{\frac{1}{2}}}{2^m m!} \sin^m \theta, \quad (32)$$

and from Eq. (31) and (25) for $n = m + 1$ we get

$$R_{m+1}^m(\theta) = (2m + 3)^{\frac{1}{2}} \cos \theta R_m^m(\theta). \quad (33)$$

The recursion relation Eq. (26) in the case of functions $R_n^m(\theta)$ is

$$\begin{aligned} R_n^m(\theta) = & \left(\frac{2n+1}{n^2-m^2} \right)^{\frac{1}{2}} \left[(2n-1)^{\frac{1}{2}} \cos \theta R_{n-1}^m(\theta) \right. \\ & \left. - \left(\frac{(n-1)^2-m^2}{2n-3} \right)^{\frac{1}{2}} R_{n-2}^m(\theta) \right] \quad \text{for } n \geq m+2. \end{aligned} \quad (34)$$

From Eq. (32)-(34) we obtain the following derivatives:

$$\frac{dR_m^m(\theta)}{d\theta} = \frac{((2-\delta_m^0)(2m+1)(2m)!)^{\frac{1}{2}}}{2^m m!} m \sin^{m-1} \theta \cos \theta, \quad (35)$$

$$\frac{dR_{m+1}^m(\theta)}{d\theta} = (2m+3)^{\frac{1}{2}} \left(\cos \theta \frac{dR_m^m(\theta)}{d\theta} - \sin \theta R_m^m(\theta) \right), \quad (36)$$

$$\begin{aligned} \frac{dR_n^m(\theta)}{d\theta} = & \left(\frac{2n+1}{n^2-m^2} \right)^{\frac{1}{2}} \left[(2n-1)^{\frac{1}{2}} \left(\cos \theta \frac{dR_{n-1}^m(\theta)}{d\theta} - \sin \theta R_{n-1}^m(\theta) \right) \right. \\ & \left. - \left(\frac{(n-1)^2-m^2}{2n-3} \right)^{\frac{1}{2}} \frac{dR_{n-2}^m(\theta)}{d\theta} \right] \quad \text{for } n \geq m+2. \end{aligned} \quad (37)$$

In geophysical research instead of $R_n^m(\theta)$, so-called Schmidt functions are widely used. They are obtained by choosing $k_{n,m}^2 = 1/(2n+1)$ in Eq. (30). Thus, denoting the Schmidt functions as $P_n^m(\theta)$, we have

$$P_n^m(\theta) = \frac{1}{(2n+1)^{1/2}} R_n^m(\theta) = \left(\frac{(2-\delta_{m,0})(n-m)!}{(n+m)!} \right)^{\frac{1}{2}} P_{n,m}(\cos \theta). \quad (38)$$

In the following we will use the Schmidt functions to write the full solution of the Laplace equation (9).

2.4 Coronal magnetic field between the Sun and the source-surface

In our considerations we restricted our attention to the coronal region where the magnetic field pressure p_B dominates and we assumed that this region is current-free ($j = 0$). Since at some distance from the Sun the solar wind starts to drag the magnetic field and forces the magnetic field lines to open, we will define a surface, termed the “source-surface”, where currents exist and cancel the transverse magnetic field. Thus, at the source-surface the magnetic field is purely radial ($\mathbf{B} = \mathbf{B}_r$). Furthermore, we will assume that this surface is spherical, with radius R_s (see Fig. 4). The location of the source-surface is usually set to $R_s = 2.5R_0$, where R_0 is the radius of the Sun [9].

To find the potential $\Psi(r, \theta, \phi)$ and the coronal magnetic field between two spheres (the Sun and the source-surface), where our current-free assumption holds, we will use results obtained for solutions of the Laplace equation. From Eq. (15) we write the radial part of the solution in the region $R_0 \leq r \leq R_s$ as (see [24] 17.13)

$$\Lambda_n = a_n R_s \left(\frac{r}{R_s} \right)^n + b_n R_0 \left(\frac{R_0}{r} \right)^{n+1}, \quad (39)$$

which with Eq. (18) and (38) gives the general solution

$$\begin{aligned} \Psi = & \sum_{n=0}^{\infty} \sum_{m=0}^n P_n^m(\theta) \left\{ g_{nm} \cos m\phi \left[R_0 \left(\frac{R_0}{r} \right)^{n+1} + s_{nm} R_s \left(\frac{r}{R_s} \right)^n \right] \right. \\ & \left. + h_{nm} \sin m\phi \left[R_0 \left(\frac{R_0}{r} \right)^{n+1} + t_{nm} R_s \left(\frac{r}{R_s} \right)^n \right] \right\}, \end{aligned} \quad (40)$$

where g_{nm} , h_{nm} , s_{nm} and t_{nm} are constants.

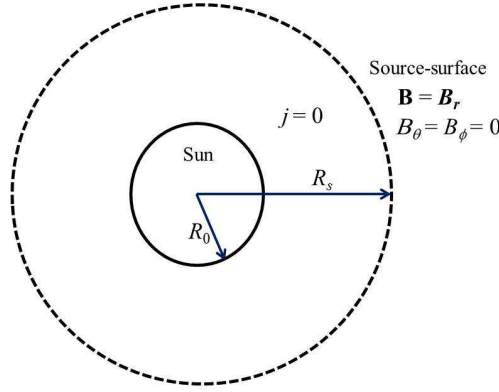


Figure 4: Geometry of the problem. We assume that between the Sun's surface (R_0) and the source-surface (R_s) the corona is current-free $j = 0$. At the source-surface the magnetic field is purely radial $\mathbf{B} = \mathbf{B}_r$.

At the source-surface $r = R_s$ the magnetic field must be purely radial, i.e. $B = B_r(R_s, \theta, \phi)$ ($B_\theta = B_\phi = 0$ for $r = R_s$). Equation (8) therefore implies that $\Psi(R_s, \theta, \phi)$ is a constant. Without loss of generality we can choose $\Psi(R_s, \theta, \phi) = 0$, which from Eq. (40) gives the constants s_{nm} and t_{nm} ,

$$s_{nm} = t_{nm} = - \left(\frac{R_0}{R_s} \right)^{n+2}.$$

Taking this into account, we can express the solution for the scalar potential $\Psi(r, \theta, \phi)$ in the region $R_0 \leq r \leq R_s$ as

$$\begin{aligned} \Psi = & \sum_{n=1}^{\infty} \left[R_0 \left(\frac{R_0}{r} \right)^{n+1} - R_s \left(\frac{R_0}{R_s} \right)^{n+2} \left(\frac{r}{R_s} \right)^n \right] \\ & \times \sum_{m=0}^n P_n^m(\theta) (g_{nm} \cos m\phi + h_{nm} \sin m\phi), \end{aligned} \quad (41)$$

which using Eq. (8) gives the magnetic field components:

$$B_r = -\frac{\partial \Psi}{\partial r} = \sum_{n=1}^{\infty} \left[(n+1) \left(\frac{R_0}{r} \right)^{n+2} + n \left(\frac{R_0}{R_s} \right)^{n+2} \left(\frac{r}{R_s} \right)^{n-1} \right] \\ \times \sum_{m=0}^n P_n^m(\theta) (g_{nm} \cos m\phi + h_{nm} \sin m\phi), \quad (42)$$

$$B_\theta = -\frac{1}{r} \frac{\partial \Psi}{\partial \theta} = -\sum_{n=1}^{\infty} \left[\left(\frac{R_0}{r} \right)^{n+2} - \left(\frac{R_0}{R_s} \right)^{n+2} \left(\frac{r}{R_s} \right)^{n-1} \right] \\ \times \sum_{m=0}^n \frac{dP_n^m(\theta)}{d\theta} (g_{nm} \cos m\phi + h_{nm} \sin m\phi), \quad (43)$$

$$B_\phi = -\frac{1}{r \sin \theta} \frac{\partial \Psi}{\partial \phi} = \sum_{n=1}^{\infty} \left[\left(\frac{R_0}{r} \right)^{n+2} - \left(\frac{R_0}{R_s} \right)^{n+2} \left(\frac{r}{R_s} \right)^{n-1} \right] \\ \times \sum_{m=0}^n P_n^m(\theta) \frac{m}{\sin \theta} (g_{nm} \sin m\phi - h_{nm} \cos m\phi). \quad (44)$$

Note that in Eq. (41)-(44) we omitted the term $n = 0$, since the requirement $\nabla \cdot \mathbf{B} = 0$ imposes that this term vanish.

To find the coefficients g_{nm} and h_{nm} in Eq. (41)-(44), we multiply Eq. (42) for the case $r = R_0$ with $P_{n'}^{m'}(\theta) \cos m'\phi$ and $P_{n'}^{m'}(\theta) \sin m'\phi$ to obtain g_{nm} and h_{nm} , respectively. By integrating over the spherical surface and using orthogonality of the Legendre polynomials with Schmidt normalization, i.e.

$$\frac{1}{4\pi} \int_0^\pi \int_0^{2\pi} P_n^m(\theta) \begin{Bmatrix} \cos m\phi \\ \sin m\phi \end{Bmatrix} P_{n'}^{m'}(\theta) \begin{Bmatrix} \cos m'\phi \\ \sin m'\phi \end{Bmatrix} \sin \theta d\theta d\phi = \frac{1}{2n+1} \delta_n^{n'} \delta_m^{m'}, \quad (45)$$

we get

$$\begin{Bmatrix} g_{nm} \\ h_{nm} \end{Bmatrix} = \frac{2n+1}{4\pi \left(n+1 + n \left(\frac{R_0}{R_s} \right)^{2n+1} \right)} \\ \times \int_0^\pi d\theta \sin \theta P_n^m(\theta) \int_0^{2\pi} d\phi B_r(R_0, \theta, \phi) \begin{Bmatrix} \cos m\phi \\ \sin m\phi \end{Bmatrix}. \quad (46)$$

Since the radial component of the photospheric magnetic field $B_r(R_0, \theta, \phi)$ in Eq. (46) can be derived from solar magnetograms, we can calculate the coefficients g_{nm} and h_{nm} , and using Eq. (42)-(44) we can obtain the coronal field in the region $R_0 \leq r \leq R_s$. To generate $P_n^m(\theta)$ and $dP_n^m(\theta)/d\theta$ for all n and m ($m \leq n$) needed in Eq. (46) and Eq. (42)-(44), we use Eq. (32)-(37) keeping in mind

$$P_n^m(\theta) = \frac{1}{(2n+1)^{1/2}} R_n^m(\theta). \quad (47)$$

The model of the coronal magnetic field based on equations derived here is referred to as a potential-field source-surface (PFSS) model [9]-[10].

3 Schatten current sheet (SCS) model

If we consider the radial solution for the coronal magnetic field which is not bounded by the source-surface, then the term r/R_s is absent in Eq. (39). Thus, for the current-free $r \geq R_0$ region, the solution for the potential $\Psi(r, \theta, \phi)$ is

$$\Psi = \sum_{n=1}^{\infty} R_0 \left(\frac{R_0}{r} \right)^{n+1} \sum_{m=0}^n P_n^m(\theta) (g_{nm} \cos m\phi + h_{nm} \sin m\phi), \quad (48)$$

which with Eq. (8) gives the magnetic field components

$$B_r = -\frac{\partial \Psi}{\partial r} = \sum_{n=1}^{\infty} (n+1) \left(\frac{R_0}{r} \right)^{n+2} \sum_{m=0}^n P_n^m(\theta) (g_{nm} \cos m\phi + h_{nm} \sin m\phi), \quad (49)$$

$$B_\theta = -\frac{1}{r} \frac{\partial \Psi}{\partial \theta} = -\sum_{n=1}^{\infty} \left(\frac{R_0}{r} \right)^{n+2} \sum_{m=0}^n \frac{dP_n^m(\theta)}{d\theta} (g_{nm} \cos m\phi + h_{nm} \sin m\phi), \quad (50)$$

$$B_\phi = -\frac{1}{r \sin \theta} \frac{\partial \Psi}{\partial \phi} = \sum_{n=1}^{\infty} \left(\frac{R_0}{r} \right)^{n+2} \sum_{m=0}^n P_n^m(\theta) \frac{m}{\sin \theta} (g_{nm} \sin m\phi - h_{nm} \cos m\phi). \quad (51)$$

The coefficients g_{nm} and h_{nm} in Eq. (48)-(51), instead of Eq. (46), are now

$$\begin{Bmatrix} g_{nm} \\ h_{nm} \end{Bmatrix} = \frac{2n+1}{4\pi(n+1)} \int_0^\pi d\theta \sin \theta P_n^m(\theta) \int_0^{2\pi} d\phi B_r(R_0, \theta, \phi) \begin{Bmatrix} \cos m\phi \\ \sin m\phi \end{Bmatrix}. \quad (52)$$

Since the solution for the coronal magnetic field Eq. (49)-(51) does not take into account the influence of plasma motion and the fact that at some distance from the Sun the condition $\beta \ll 1$ is violated, it cannot represent the coronal field for all $r \geq R_0$. To include the effect of plasma currents on the structure of the solar corona, but not with the zero potential source-surface, Schatten proposed the introduction of a new spherical source-surface at $r = R_{cp}$, which we call the cusp surface, from where the transverse currents are allowed [12]. These currents are limited to thin sheets between regions of opposite magnetic polarity where the Lorenz force $\mathbf{j} \times \mathbf{B}$ is small. While the PFSS zero potential source-surface forces magnetic field lines to be radial at $r = R_s$, the Schatten current sheet (SCS) model allows a non-radial structure of the coronal field for $r \geq R_{cp}$. The SCS model better agrees with coronal observations. In particular, with the observations of polar plumes and streamers [12].

3.1 Coronal magnetic field beyond the source-surface

In the SCS model the coronal magnetic field is calculated first in the region $R_0 \leq r \leq R_{cp}$. The obtained solution is then reoriented at $r = R_{cp}$ to point outward. This reorientation of the field means that if $B_r(R_{cp}) \geq 0$ no changes are needed, but if $B_r(R_{cp}) < 0$, the signs of the $B_r(R_{cp})$, $B_\theta(R_{cp})$ and $B_\phi(R_{cp})$ components are changed. The field beyond R_{cp} is obtained by matching the potential-field solution for $r \geq R_{cp}$, i.e.

$$B_r = -\frac{d\Psi}{dr} = \sum_{n=0}^{\infty} (n+1) \left(\frac{R_{cp}}{r}\right)^{n+2} \sum_{m=0}^n P_n^m(\theta) (g'_{nm} \cos m\phi + h'_{nm} \sin m\phi), \quad (53)$$

$$B_\theta = -\frac{1}{r} \frac{d\Psi}{d\theta} = -\sum_{n=0}^{\infty} \left(\frac{R_{cp}}{r}\right)^{n+2} \sum_{m=0}^n \frac{dP_n^m(\theta)}{d\theta} (g'_{nm} \cos m\phi + h'_{nm} \sin m\phi), \quad (54)$$

$$B_\phi = -\frac{1}{r \sin \theta} \frac{d\Psi}{d\phi} = \sum_{n=0}^{\infty} \left(\frac{R_{cp}}{r}\right)^{n+2} \sum_{m=0}^n P_n^m(\theta) \frac{m}{\sin \theta} (g'_{nm} \sin m\phi - h'_{nm} \cos m\phi), \quad (55)$$

with the magnetic field components of the reoriented field at $r = R_{cp}$. The effect of this step is to open magnetic field lines, so that no closed magnetic lines exist beyond R_{cp} . Although the reorientation of the magnetic field at R_{cp} violates $\nabla \cdot \mathbf{B} = 0$ this does not affect the magnetic stress. The final step is to assign proper polarity to the magnetic field lines in the region $r \geq R_{cp}$ using the polarity obtained before the field reorientation at R_{cp} . This polarity restoration ensures that $\nabla \cdot \mathbf{B} = 0$ is not violated. Furthermore, it implies that current sheets are introduced between the magnetic fields of opposite polarity.

It should be pointed out that calculation of the coronal field in the region $R_0 \leq r \leq R_{cp}$ based on Eq. (49)-(51) and with $R_{cp} = 1.6R_0$ is proposed by Schatten. However, Schatten's idea to introduce current sheets using the technique described above is used in different models. For example, the Wang-Sheeley-Argue (WSA) solar wind model uses the PFSS model to obtain a coronal field solution for $R_0 \leq r \leq R_s$ Eq. (42)-(44), and then employs the SCS model to derive the solution beyond $r \geq R_s$ (i.e. in this case the assumption is that $R_{cp} = R_s$) [14], [26]. The WSA model with an extension of the coronal magnetic field to $\sim 25R_0$, based on the SCS model, is used to provide the inner solar wind boundary conditions for the ENLIL MHD code [20]. In the coupling of the PFSS and SCS models, R_{cp} can be set below R_s . One of the benefits of using $R_{cp} < R_s$ is to remove kinks in the field lines at the interference of the models [27]. Further, Zhao and Hoeksema in their coronal field model which includes horizontal volume currents, for example, used the SCS technique to derive the magnetic field between R_{cp} and R_s ($R_{cp} < R_s$) [28], [29].

To derive coefficients g'_{nm} and h'_{nm} in an overdetermined system of equations Eq. (53)-(55) we use a least-squares procedure to fit the magnetic field components Eq. (53)-(55) at R_{cp} to those obtained by the field reorientation. Let us denote the reoriented field at R_{cp} as $B_k^{cp}(\theta_i, \phi_j)$, where $k = 1, 2, 3$ corresponds to r, θ, ϕ , respectively (see e.g. [12], [28], [29]). Here, we express the quantities on a uniform mesh with grid points θ_i and ϕ_j ($i \in [1, I], j \in [1, J]$), and we limit the degree n of the harmonics by N_s .

In the least-squares approach, we are looking for g'_{nm} and h'_{nm} so that the sum of squared residuals

$$F = \sum_{k=1}^3 \sum_{i=1}^I \sum_{j=1}^J \left[B_k^{cp}(\theta_i, \phi_j) - \sum_{n=0}^{N_s} \sum_{m=0}^n (g'_{nm} \alpha_{knm}(\theta_i, \phi_j) + h'_{nm} \beta_{knm}(\theta_i, \phi_j)) \right]^2, \quad (56)$$

is minimized,

$$\frac{\partial F}{\partial g'_{nm}} = 0 \quad \text{and} \quad \frac{\partial F}{\partial h'_{nm}} = 0. \quad (57)$$

In Eq. (56) we use symbols α and β , where

$$\begin{aligned} \alpha_{1nm}(\theta_i, \phi_j) &= (n+1)P_n^m(\theta_i) \cos m\phi_j, \\ \alpha_{2nm}(\theta_i, \phi_j) &= - \left. \frac{dP_n^m(\theta)}{d\theta} \right|_{\theta=\theta_i} \cos m\phi_j, \\ \alpha_{3nm}(\theta_i, \phi_j) &= \frac{m}{\sin \theta_i} P_n^m(\theta_i) \sin m\phi_j, \\ \beta_{1nm}(\theta_i, \phi_j) &= (n+1)P_n^m(\theta_i) \sin m\phi_j, \\ \beta_{2nm}(\theta_i, \phi_j) &= - \left. \frac{dP_n^m(\theta)}{d\theta} \right|_{\theta=\theta_i} \sin m\phi_j, \\ \beta_{3nm}(\theta_i, \phi_j) &= \frac{m}{\sin \theta_i} P_n^m(\theta_i) \cos m\phi_j, \end{aligned} \quad (58)$$

as follows from Eq. (53)-(55). From Eq. (56) and (57) for each (m, n) we get

$$\sum_{k=1}^3 \sum_{i=1}^I \sum_{j=1}^J \alpha_{knm}(\theta_i, \phi_j) \left[B_k^{cp}(\theta_i, \phi_j) - \sum_{p=0}^{N_s} \sum_{t=0}^p \left(g'_{pt} \alpha_{kpt}(\theta_i, \phi_j) + h'_{pt} \beta_{kpt}(\theta_i, \phi_j) \right) \right] = 0, \quad (59)$$

and

$$\sum_{k=1}^3 \sum_{i=1}^I \sum_{j=1}^J \beta_{knm}(\theta_i, \phi_j) \left[B_k^{cp}(\theta_i, \phi_j) - \sum_{p=0}^{N_s} \sum_{t=0}^p \left(g'_{pt} \alpha_{kpt}(\theta_i, \phi_j) + h'_{pt} \beta_{kpt}(\theta_i, \phi_j) \right) \right] = 0. \quad (60)$$

This can be written in a matrix form as

$$\widehat{\alpha\beta} \cdot \widehat{B} = \widehat{\alpha\beta} \cdot \widehat{\alpha\beta}^T \cdot \widehat{GH}, \quad (61)$$

where

$$\widehat{B} = \begin{bmatrix} B_1^{cp}(\theta_1, \phi_1) \\ B_1^{cp}(\theta_1, \phi_2) \\ \vdots \\ B_1^{cp}(\theta_1, \phi_J) \\ B_1^{cp}(\theta_2, \phi_1) \\ \vdots \\ B_1^{cp}(\theta_I, \phi_J) \\ B_2^{cp}(\theta_1, \phi_1) \\ \vdots \\ B_3^{cp}(\theta_I, \phi_J) \end{bmatrix}, \quad \widehat{GH} = \begin{bmatrix} g_{00} \\ g_{10} \\ g_{11} \\ g_{20} \\ \vdots \\ \vdots \\ g_{N_s, N_s} \\ h_{11} \\ h_{21} \\ h_{22} \\ \vdots \\ \vdots \\ h_{N_s, N_s} \end{bmatrix}, \quad (62)$$

$$\widehat{\alpha\beta} = \begin{bmatrix}
\alpha_{100}(\theta_1, \phi_1) & \alpha_{100}(\theta_1, \phi_2) & \cdot & \cdot & \alpha_{100}(\theta_1, \phi_J) & \alpha_{100}(\theta_2, \phi_1) & \cdot \\
\alpha_{110}(\theta_1, \phi_1) & \alpha_{110}(\theta_1, \phi_2) & \cdot & \cdot & \alpha_{110}(\theta_1, \phi_J) & \alpha_{110}(\theta_2, \phi_1) & \cdot \\
\alpha_{111}(\theta_1, \phi_1) & \alpha_{111}(\theta_1, \phi_2) & \cdot & \cdot & \alpha_{111}(\theta_1, \phi_J) & \alpha_{111}(\theta_2, \phi_1) & \cdot \\
\alpha_{120}(\theta_1, \phi_1) & \alpha_{120}(\theta_1, \phi_2) & \cdot & \cdot & \alpha_{120}(\theta_1, \phi_J) & \alpha_{120}(\theta_2, \phi_1) & \cdot \\
\cdot & \cdot & \cdot & \cdot & \cdot & \cdot & \cdot \\
\cdot & \cdot & \cdot & \cdot & \cdot & \cdot & \cdot \\
\alpha_{1N_s N_s}(\theta_1, \phi_1) & \alpha_{1N_s N_s}(\theta_1, \phi_2) & \cdot & \cdot & \alpha_{1N_s N_s}(\theta_1, \phi_J) & \alpha_{1N_s N_s}(\theta_2, \phi_1) & \cdot \\
\beta_{111}(\theta_1, \phi_1) & \beta_{111}(\theta_1, \phi_2) & \cdot & \cdot & \beta_{111}(\theta_1, \phi_J) & \beta_{111}(\theta_2, \phi_1) & \cdot \\
\beta_{121}(\theta_1, \phi_1) & \beta_{121}(\theta_1, \phi_2) & \cdot & \cdot & \beta_{121}(\theta_1, \phi_J) & \beta_{121}(\theta_2, \phi_1) & \cdot \\
\beta_{122}(\theta_1, \phi_1) & \beta_{122}(\theta_1, \phi_2) & \cdot & \cdot & \beta_{122}(\theta_1, \phi_J) & \beta_{122}(\theta_2, \phi_1) & \cdot \\
\cdot & \cdot & \cdot & \cdot & \cdot & \cdot & \cdot \\
\cdot & \cdot & \cdot & \cdot & \cdot & \cdot & \cdot \\
\beta_{1N_s N_s}(\theta_1, \phi_1) & \beta_{1N_s N_s}(\theta_1, \phi_2) & \cdot & \cdot & \beta_{1N_s N_s}(\theta_1, \phi_J) & \beta_{1N_s N_s}(\theta_2, \phi_1) & \cdot \\
\cdot & \beta_{100}(\theta_I, \phi_J) & \beta_{200}(\theta_1, \phi_1) & \cdot & \cdot & \beta_{300}(\theta_I, \phi_J) & \cdot \\
\cdot & \beta_{110}(\theta_I, \phi_J) & \beta_{210}(\theta_1, \phi_1) & \cdot & \cdot & \beta_{310}(\theta_I, \phi_J) & \cdot \\
\cdot & \beta_{111}(\theta_I, \phi_J) & \beta_{211}(\theta_1, \phi_1) & \cdot & \cdot & \beta_{311}(\theta_I, \phi_J) & \cdot \\
\cdot & \beta_{120}(\theta_I, \phi_J) & \beta_{220}(\theta_1, \phi_1) & \cdot & \cdot & \beta_{3210}(\theta_I, \phi_J) & \cdot \\
\cdot & \cdot & \cdot & \cdot & \cdot & \cdot & \cdot \\
\cdot & \cdot & \cdot & \cdot & \cdot & \cdot & \cdot \\
\cdot & \alpha_{1N_s N_s}(\theta_I, \phi_J) & \alpha_{2N_s N_s}(\theta_1, \phi_1) & \cdot & \cdot & \alpha_{3N_s N_s}(\theta_I, \phi_J) & \cdot \\
\cdot & \beta_{111}(\theta_I, \phi_J) & \beta_{211}(\theta_1, \phi_1) & \cdot & \cdot & \beta_{311}(\theta_I, \phi_J) & \cdot \\
\cdot & \beta_{121}(\theta_I, \phi_J) & \beta_{221}(\theta_1, \phi_1) & \cdot & \cdot & \beta_{321}(\theta_I, \phi_J) & \cdot \\
\cdot & \beta_{122}(\theta_I, \phi_J) & \beta_{222}(\theta_1, \phi_1) & \cdot & \cdot & \beta_{322}(\theta_I, \phi_J) & \cdot \\
\cdot & \cdot & \cdot & \cdot & \cdot & \cdot & \cdot \\
\cdot & \cdot & \cdot & \cdot & \cdot & \cdot & \cdot \\
\cdot & \beta_{1N_s N_s}(\theta_I, \phi_J) & \beta_{2N_s N_s}(\theta_1, \phi_1) & \cdot & \cdot & \beta_{3N_s N_s}(\theta_I, \phi_J) & \cdot
\end{bmatrix}. \quad (63)$$

Here, the dimension of \widehat{B} is $(3IJ) \times 1$, the dimension of \widehat{GH} is $(N_s + 1)^2 \times 1$, and $\widehat{\alpha\beta}$ is a $(N_s + 1)^2 \times (3IJ)$ matrix. In \widehat{GH} we omitted all $m = 0$ elements ($\sin m\phi = 0$ in Eq. (53)-(55), for $m = 0$). In Eq. (61) $\widehat{\alpha\beta}^T$ is the transpose matrix of $\widehat{\alpha\beta}$ with the dimension $(3IJ) \times (N_s + 1)^2$. Substituting $\widehat{AB} = \widehat{\alpha\beta} \cdot \widehat{\alpha\beta}^T$, from Eq. (61) we obtain the solution for g'_{nm} and h'_{nm}

$$\widehat{GH} = \widehat{AB}^{-1} \cdot \widehat{\alpha\beta} \cdot \widehat{B}, \quad (64)$$

where \widehat{AB}^{-1} is the inverse of $(N_s + 1)^2 \times (N_s + 1)^2$ \widehat{AB} matrix. The coefficients g'_{nm} and h'_{nm} obtained from Eq. (64) are used in the discrete form of Eq. (53)-(55) to calculate the field for $r \geq R_{cp}$. At the end, since this solution has all magnetic field lines pointing outward, the polarity of magnetic field lines in the $r \geq R_{cp}$ region is restored to match the polarity of the $R_0 \leq r \leq R_{cp}$ coronal field solution.

4 Numerical solutions with GONG magnetograms

A Fortran numerical code has been developed to calculate the coronal magnetic field in $R_0 \leq r \leq R_s$ and $r \geq R_s$ regions using the PFSS and SCS models, respectively. To obtain the spherical harmonic coefficients g_{nm} and h_{nm} Eq. (46), GONG standard magnetograms are used [6]. The magnetograms represent full-surface (synoptic) maps of the photospheric magnetic field $B_r(R_0, \theta, \phi)$ measured in Gauss [G], and are available as full Carrington rotation maps (see e.g. Fig. 3), or as near-real-time hourly updated magnetograms. The magnetograms are given on the $\sin(\theta) - \phi$ grid with 180×360 grid points, and are provided in the FITS data format. The CFITSIO library is used to process the FITS files and extract the data [30].

In the following we will examine numerical results obtained for different choices of numerical parameters. To capture cases with different solar activity levels, we will use the CR2077 and CR2147 magnetograms shown in Fig. 3. These magnetograms cover the activity at solar minimum (CR2077) and maximum (CR2147).

4.1 Number of spherical harmonics

The original GONG magnetograms are uniform on the $\sin(\theta) - \phi$ mesh and do not include grid points at the poles. We will investigate the consequences of using the magnetograms in this form to obtain g_{nm} and h_{nm} coefficients Eq. (46), and to derive the coronal magnetic field Eq. (42)-(44). To calculate the coefficients, we use the discretized form of Eq. (46),

$$\begin{Bmatrix} g_{nm} \\ h_{nm} \end{Bmatrix} = \frac{2n+1}{4\pi \left(n+1 + n \left(\frac{R_0}{R_s} \right)^{2n+1} \right)} \sum_{i=1}^{N_\theta^\circ} \sum_{j=1}^{N_\phi^\circ} \Delta A_{ij} P_n^m(\theta_i) B_r(R_0, \theta_i, \phi_j) \begin{Bmatrix} \cos m\phi_j \\ \sin m\phi_j \end{Bmatrix}, \quad (65)$$

where $\Delta A_{ij} = \Delta \cos \theta \Delta \phi = 4\pi / (N_\theta^\circ N_\phi^\circ)$ for the uniform $\sin(\theta) - \phi$ mesh, with $N_\theta^\circ = 180$ and $N_\phi^\circ = 360$ for GONG magnetograms. Furthermore, instead of using an infinite n sum in Eq. (42)-(44), we will limit the maximum degree of harmonics with N .

Since the radial component of the magnetic field Eq. (42) obtained by the PFSS model should match the magnetic field of the original magnetogram for $r = R_0$, in Fig. 5 we plot (a) the original CR2077 magnetogram, and the solutions for $B_r(R_0, \theta, \phi)$ from the model for (b) $N = 60$, (c) $N = 90$, and (d) $N = 120$. The source-surface in the PFSS model is placed at $R_s = 2.5R_0$. The magnetic field scale in the figure is saturated at ± 15 G. Fig. 6 represent the same case but with the CR2147 magnetogram. Note that the original magnetograms do not include the poles, while we included them in the PFSS solution. As we can see from (a) to (d) comparison, the fine details are blurred out for solutions with a low number of harmonics and a series of ring-like structures are present. These structures are induced by a large abrupt difference in the observed magnetic field (see e.g. [31]). As it can be seen from Fig. 5 and 6, the ringing effect is more pronounced in the case of magnetograms with strong active regions than in the case of “quiet” magnetograms. Increasing the number of harmonics, i.e. N , decreases

this effect. However, with increasing N , an artificial field emerges in the polar regions. Using unsigned magnetic flux

$$\Phi(r) = r^2 \int_0^\pi \int_0^{2\pi} |B_r(r, \theta, \phi)| \sin \theta d\theta d\phi \quad (66)$$

we can obtain the difference $|\Phi^o(R_0) - \Phi^N(R_0)|/\Phi^o(R_0)$ at R_0 between the original magnetogram $\Phi^o(R_0)$, and the results $\Phi^N(R_0)$ obtained with different N used in the PFSS model. The difference is $\approx 18\%$, $\approx 10\%$ and $\approx 7\%$ for CR2077 and $N = 60$, $N = 90$ and $N = 120$, respectively. For CR2147 we have $\approx 9\%$, $\approx 7\%$ and $\approx 4\%$ for $N = 60$, $N = 90$ and $N = 120$, respectively. As we can see, with increasing N , the difference in fluxes decreases for both the CR2077 and CR2147 magnetograms.

While using a high number of harmonics at the photospheric level has obvious positive and negative effects, at the source-surface there is little difference in the results obtained using different N . This can be expected since the radial part in Eq. (42)-(44) decreases with n . Thus, the higher degree harmonics are losing their importance with increasing distance from the Sun. To illustrate this, in Fig. 7 and 8 we can see solutions for the magnetic field at the source-surface $B_r(2.5R_0, \theta, \phi)$ obtained with (a) $N = 60$, (b) $N = 90$, and (c) $N = 120$, for the CR2077 (Fig. 7) and CR2147 (Fig. 8) magnetograms. In both cases, CR2077 and CR2147, the difference between unsigned magnetic fluxes at the source-surface, e.g. $|\Phi^{60}(R_s) - \Phi^{120}(R_s)|/\Phi^{60}(R_s)$, is negligible.

Knowing the coronal magnetic field in the region $R_0 \leq r \leq R_s$, Eq. (42)-(44), we can trace the magnetic field lines using the following equations:

$$\frac{dr}{ds} = \frac{B_r}{B}, \quad (67)$$

$$\frac{r d\theta}{ds} = \frac{B_\theta}{B}, \quad (68)$$

$$\frac{r \sin \theta d\phi}{ds} = \frac{B_\phi}{B}, \quad (69)$$

where ds is a segment along the field line. We use a second-order Runge-Kutta method to trace open magnetic field lines and we calculate their flux tube expansion factors f_s ,

$$f_s = \frac{|B(R_0)| R_0^2}{|B(R_s)| R_s^2}. \quad (70)$$

In Fig. 9 and 10, we plot the results obtained by tracing open coronal magnetic field lines (i.e. the lines that reach R_s) for the CR2077 (Fig. 9) and CR2147 (Fig. 10) magnetograms with (a) $N = 60$, (b) $N = 90$, and (c) $N = 120$ in the PFSS model. The red and blue colour, i.e. $1/F_s$ which is associated with the magnetic polarity and $1/f_s$ ($F_s = \text{sign}(B) f_s$), represents the foot-points of all open magnetic field lines. These foot-points we will refer to as derived COHO. The black lines represent open field lines which connect the sub-Earth positions at R_s with the foot-points at the photosphere. The sub-Earth locations in (r, θ, ϕ) coordinates are calculated using astronomical formulae for a given Carrington longitude, i.e. time and date [32].

As we can see from Fig. 9 and 10, although the derived COHO are dependent on N , in particular in the polar regions, the magnetic field lines that connect the sub-Earth positions do not show much difference. This is due to the fact that the foot-points of open magnetic field lines which connect the sub-Earth positions lie below the polar regions where the artificial magnetic fields are generated.

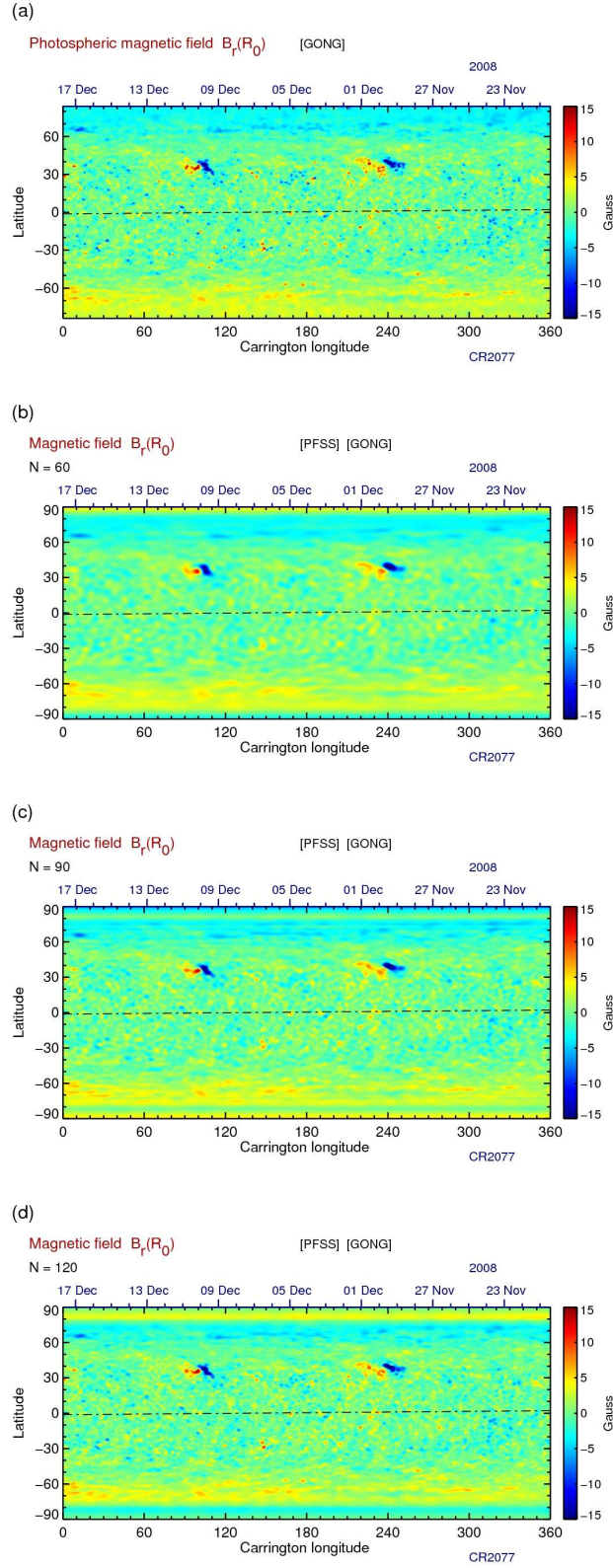


Figure 5: Magnetic field $B_r(R_0, \theta, \phi)$ from (a) the CR2077 magnetogram, and from the PFSS model with (b) $N = 60$, (c) $N = 90$, and (d) $N = 120$. The field is saturated at ± 15 G. Dash-dot line represents the sub-Earth positions.

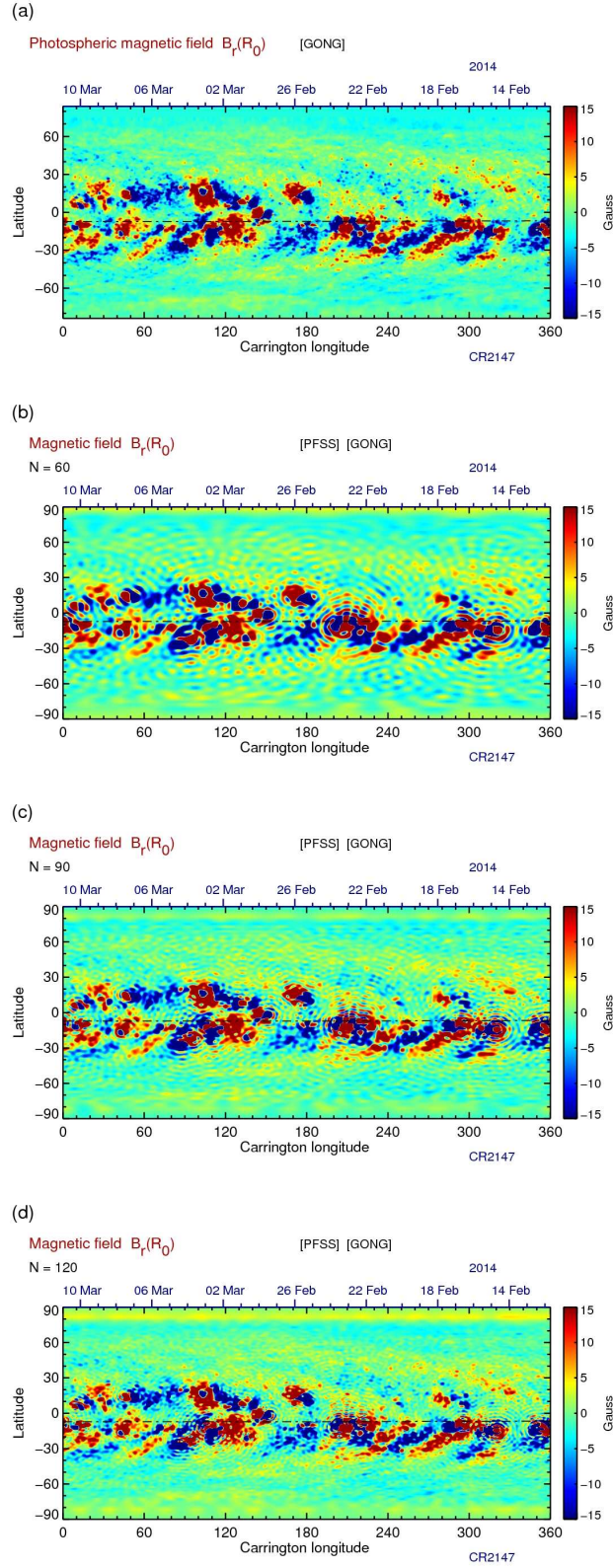


Figure 6: Magnetic field $B_r(R_0, \theta, \phi)$ from (a) the CR2147 magnetogram, and from the PFSS model with (b) $N = 60$, (c) $N = 90$, and (d) $N = 120$. The field is saturated at ± 15 G. Dash-dot line represents the sub-Earth positions.

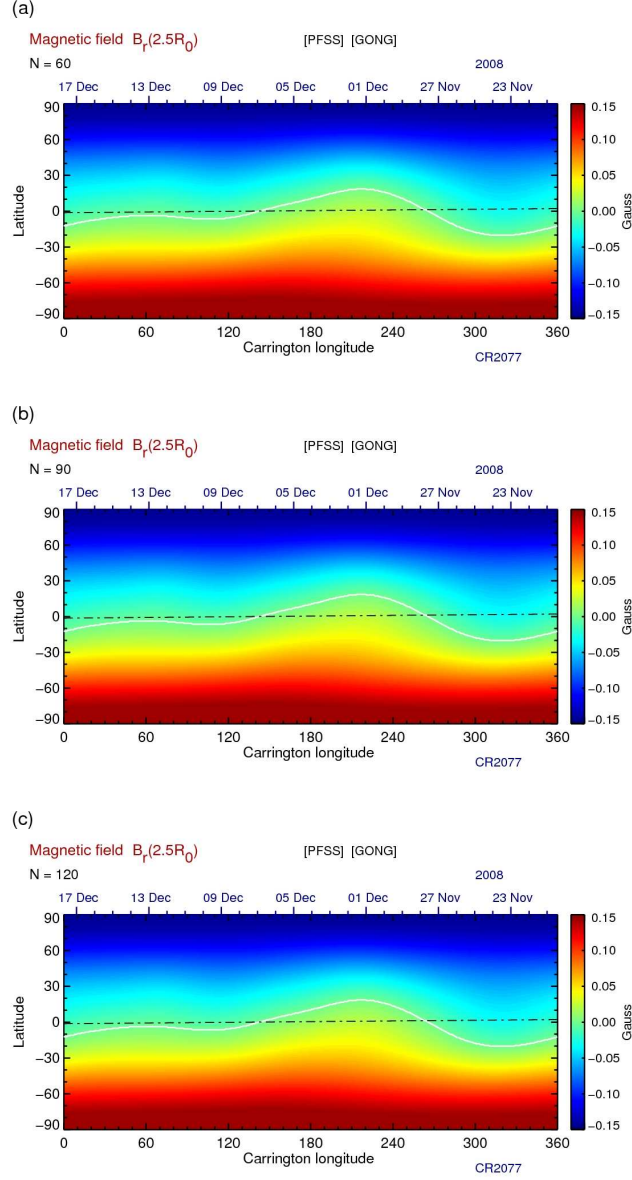


Figure 7: Magnetic field at the source-surface $B_r(2.5R_0, \theta, \phi)$ for CR2077 from the PFSS model with (a) $N = 60$, (b) $N = 90$, and (c) $N = 120$. The field is saturated at ± 0.15 G. White line represents the neutral line and dash-dot line denotes the sub-Earth positions.

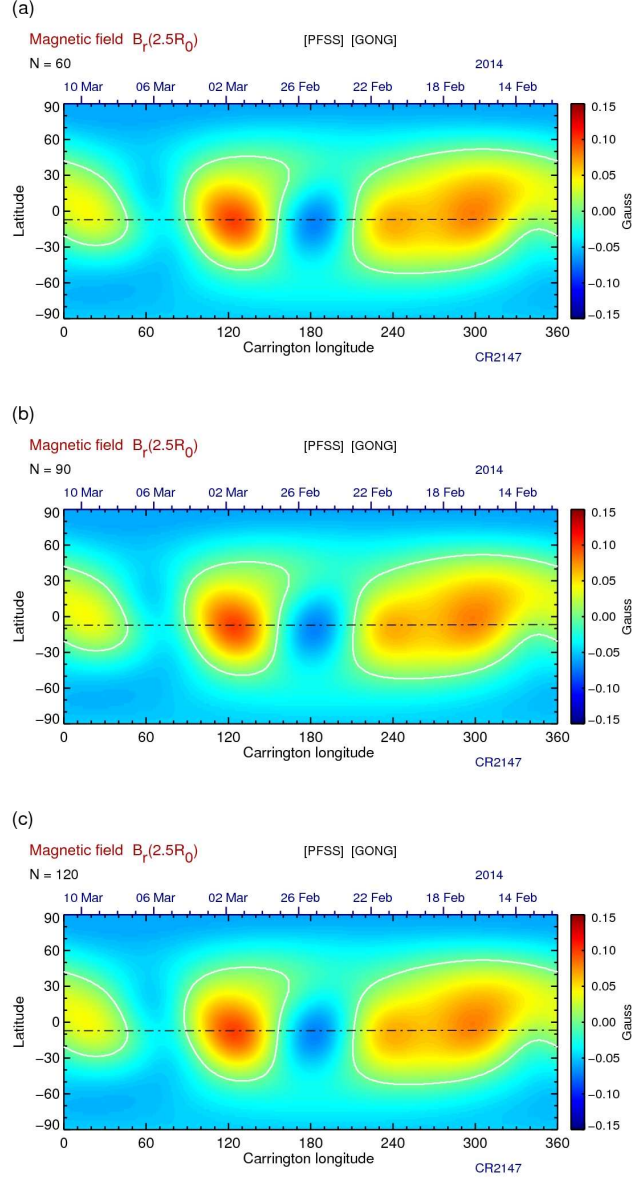


Figure 8: Magnetic field at the source-surface $B_r(2.5R_0, \theta, \phi)$ for CR2147 from the PFSS model with (a) $N = 60$, (b) $N = 90$, and (c) $N = 120$. The field is saturated at ± 0.15 G. White line represents the neutral line and dash-dot line denotes the sub-Earth positions.

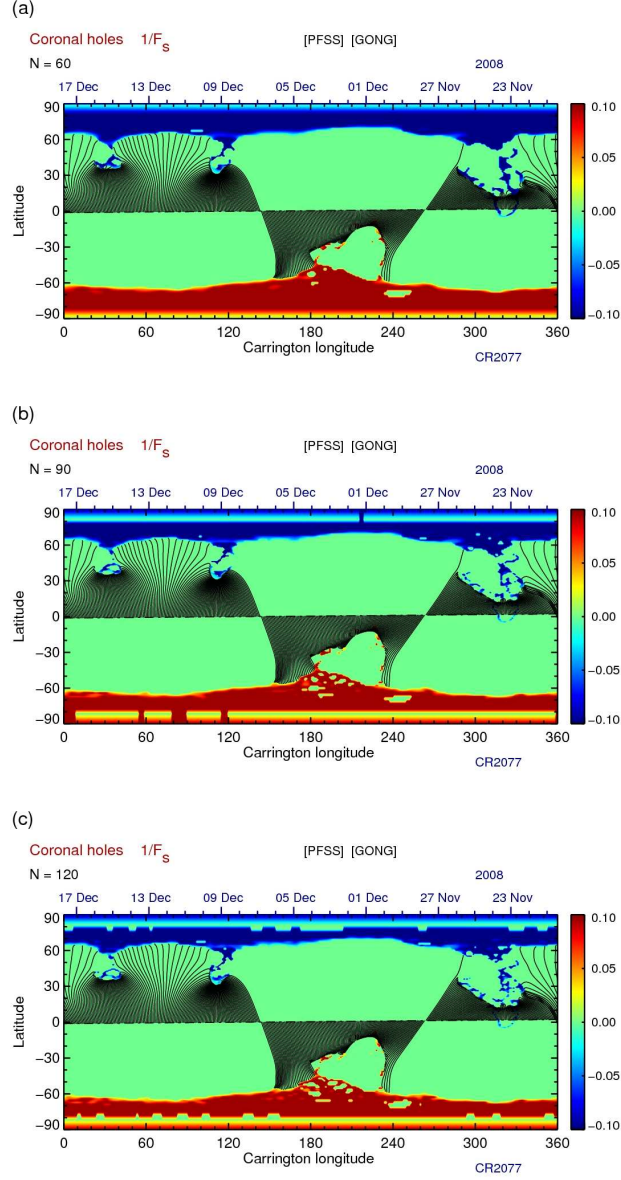


Figure 9: Derived COHO for CR2077 from the PFSS model with (a) $N = 60$, (b) $N = 90$, and (c) $N = 120$. $1/F_s$ is saturated at ± 0.1 . The black lines represent open magnetic field lines which connect the sub-Earth positions with COHO.

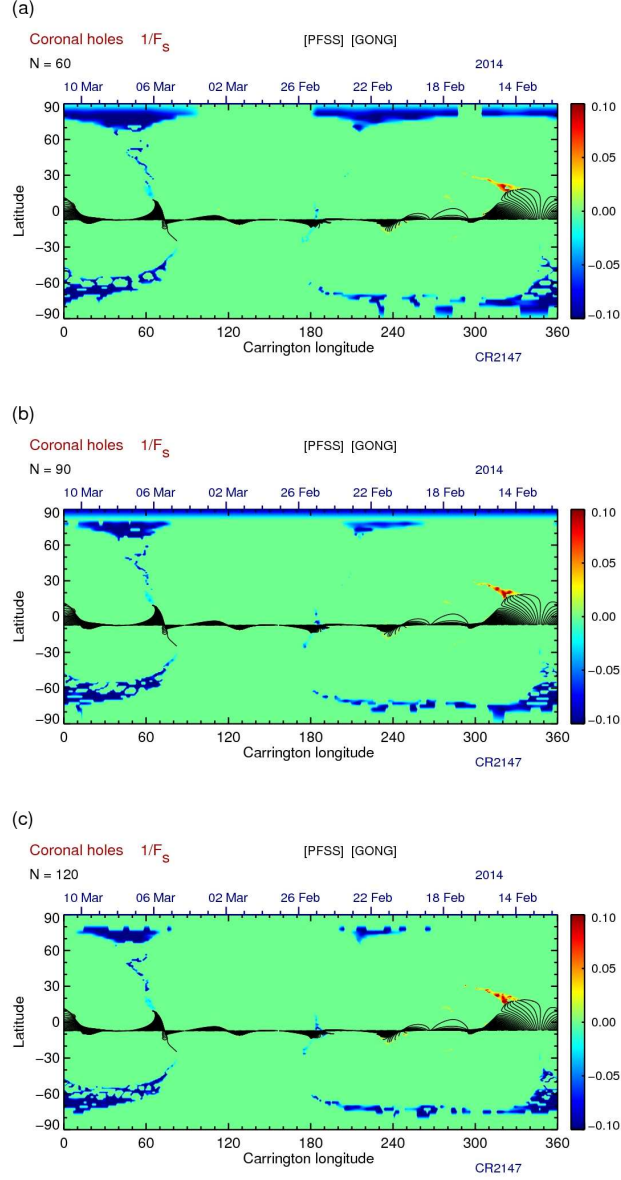


Figure 10: Derived COHO for CR2147 from the PFSS model with (a) $N = 60$, (b) $N = 90$, and (c) $N = 120$. $1/F_s$ is saturated at ± 0.1 . The black lines represent open magnetic field lines which connect the sub-Earth positions with COHO.

4.2 Re-meshed magnetograms

To improve the accuracy of the PFSS model, instead of using the original GONG magnetograms with the $\sin(\theta) - \phi$ mesh, we re-mesh the magnetograms to a uniform $\theta - \phi$ grid [31], [33], [34]. The new mesh includes the grid at the poles and contains an odd number of θ grid points. Let us denote with N_θ^o , the number of grid points for the original magnetogram, and with N_θ , the number of odd grid points for the re-meshed magnetogram. The number of ϕ grid points N_ϕ , is the same. In the following we will use the superscript o to denote the original magnetogram.

Since the new mesh contains the poles, we extend the original magnetogram to include them. The magnetic field at the south B_S and north B_N pole is approximated using the magnetic field from the θ boundaries of the original magnetogram $B_{1^o,j}^o$ and $B_{N_\theta^o,j}^o$, i.e.

$$B_S = \frac{1}{N_\phi} \sum_{j=1}^{N_\phi} B_{1^o,j}^o, \quad (71)$$

$$B_N = \frac{1}{N_\phi} \sum_{j=1}^{N_\phi} B_{N_\theta^o,j}^o. \quad (72)$$

The colatitudes of the re-meshed magnetogram are defined as

$$\theta_i = \pi \frac{N_\theta - i}{N_\theta - 1}, \quad (73)$$

where $i \in [1, N_\theta]$. We use linear interpolation to assign the magnetic field to the re-meshed magnetogram,

$$B_{i,j} = \alpha B_{i^o+1,j}^o + (1 - \alpha) B_{i^o,j}^o, \quad (74)$$

for all $j \in [1, N_\phi]$. Here

$$\alpha = \frac{\theta_{i^o}^o - \theta_i}{\delta}, \quad (75)$$

with $\theta_{i^o}^o \geq \theta_i \geq \theta_{i^o+1}^o$ and $\delta = \theta_i - \theta_{i+1}$.

To calculate Eq. (46) with the re-meshed magnetograms we use the Clenshaw-Curtis quadrature rule

$$\int_0^\pi d\theta \sin \theta F(\theta) \approx \sum_{i=1}^{N_\theta} \epsilon_i w_i F(\theta_i), \quad (76)$$

where $\epsilon_1 = \epsilon_{N_\theta} = 1/2$, and $\epsilon_i = 1$ for $i \neq 1, N_\theta$ [31]. The Clenshaw-Curtis weights w_i are

$$w_i = -\frac{2}{H} \sum_{k=0}^H \frac{\epsilon'_k}{4k^2 - 1} \cos\left(\frac{\pi k(i-1)}{H}\right), \quad (77)$$

where $H = (N_\theta - 1)/2$, $\epsilon'_0 = \epsilon'_H = 1/2$, and $\epsilon'_k = 1$ for $k \neq 1, H$. Thus, for the re-meshed magnetograms we write Eq. (46) in the discrete representation as

$$\begin{aligned} \begin{Bmatrix} g_{nm} \\ h_{nm} \end{Bmatrix} &= \frac{2n+1}{4\pi \left(n+1 + n \left(\frac{R_0}{R_s} \right)^{2n+1} \right)} \\ &\times \frac{2\pi}{N_\phi} \sum_{i=1}^{N_\theta} \sum_{j=1}^{N_\phi} \epsilon_i w_i P_n^m(\theta_i) B_r(R_0, \theta_i, \phi_j) \begin{Bmatrix} \cos m\phi_j \\ \sin m\phi_j \end{Bmatrix}. \end{aligned} \quad (78)$$

In Fig. 11-18 we show results obtained by the re-meshed magnetograms for various numerical parameters. In particular, in Fig. 11 and 12, we compare (a) the original 180×360 magnetogram with the re-meshed magnetograms using $N_\phi = 360$ and (b) $N_\theta = 181$, and (c) $N_\theta = 283$ grid points, for CR2077 (Fig. 11) and CR2147 (Fig. 12). In the case of CR2077, the difference at R_0 between the unsigned magnetic fluxes for the original magnetogram $\Phi^o(R_0)$ and the re-meshed magnetograms, i.e. $|\Phi^o(R_0) - \Phi^R(R_0)|/\Phi^o(R_0)$, is $\approx 4\%$ for both cases, with $N_\theta = 181$ and $N_\theta = 283$ grid points. For the CR2147 case, the difference is $\approx 1\%$ also for both, $N_\theta = 181$ and $N_\theta = 283$.

To examine how well the radial component of the magnetic field obtained by the PFSS model matches the re-meshed magnetogram, in Fig. 13 and 14 we plot (a) the re-meshed magnetogram, and the PFSS solutions for $B_r(R_0, \theta, \phi)$ obtained with (b) $N = 120$, (c) $N = 150$, and (d) $N = 250$. The number of grid points is $N_\theta = 181$ and $N_\phi = 360$. Figures 13 and 14 represent CR2077 and CR2147 cases respectively. Although we can notice a small ringing effect, in particular for CR2147, the re-meshed magnetogram is well represented for all choices of N_θ . We can see that the re-meshed magnetogram allows use of a larger number of spherical harmonics without causing an artificial field in the polar regions. We note that the limit imposed on N , i.e. $N \leq 2N_\theta/3$ and $N \leq N_\phi/3$, is violated in (c) and (d) [31], [34]. However, the results do not show noticeable artifacts. The difference $|\Phi^R(R_0) - \Phi^{RN}(R_0)|/\Phi^R(R_0)$ between unsigned fluxes of the re-meshed CR2077 magnetogram $\Phi^R(R_0)$ and the fluxes obtained using $B_r(R_0, \theta, \phi)$ from the PFSS model $\Phi^{RN}(R_0)$ is $\approx 3\%$, $\approx 1\%$, and $< 1\%$ for $N = 120$, $N = 150$, and $N = 250$, respectively. For the CR2147 case this difference is $\approx 3\%$, $\approx 1\%$, and $< 1\%$ for $N = 120$, $N = 150$, and $N = 250$, respectively.

For $B_r(2.5R_0, \theta, \phi)$ obtained by the PFSS model at the source-surface, there is a negligible difference in the results obtained with (a) $N = 120$, (b) $N = 150$, and (c) $N = 250$. This can be seen in Fig. 15 and 16 where re-meshed CR2077 and CR2147 magnetograms, respectively, are used in the PFSS model. The small difference is also in the results for derived COHO and open magnetic field lines which connect the photosphere with the sub-Earth locations at R_s . In Fig. 17 (CR2077) and 18 (CR2147) we can see these results for (a) $N = 120$, (b) $N = 150$, and (c) $N = 250$.

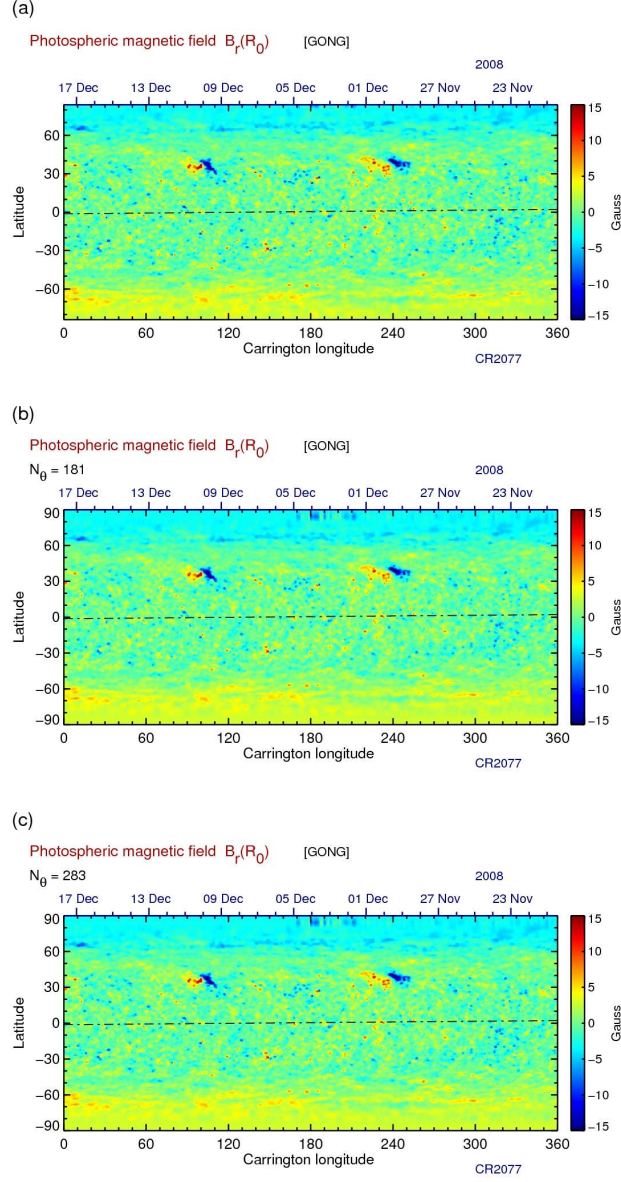


Figure 11: Photospheric radial component of the magnetic field $B_r(R_0, \theta, \phi)$ from (a) the original 180×360 CR2077 magnetogram and re-meshed magnetograms with $N_\phi = 360$ and (b) $N_\theta = 181$, and (c) $N_\theta = 283$. The field scale is saturated at ± 15 G. Dash-dot line represents the sub-Earth positions.

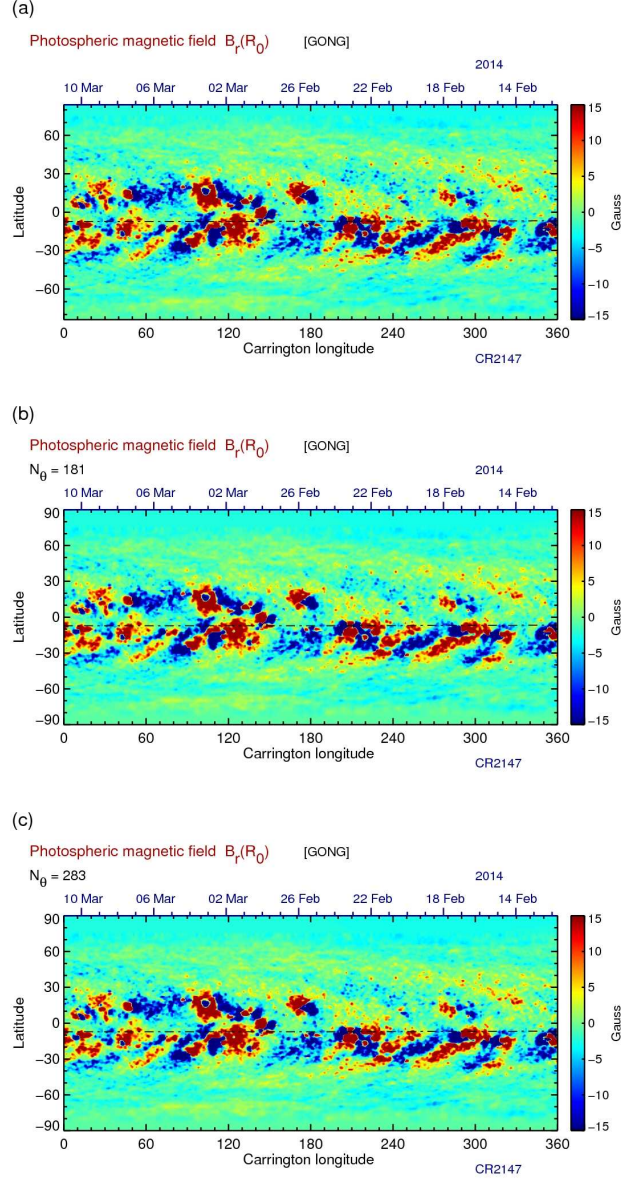


Figure 12: Photospheric radial component of the magnetic field $B_r(R_0, \theta, \phi)$ from (a) the original 180×360 CR2147 magnetogram and re-meshed magnetograms with $N_\phi = 360$ and (b) $N_\theta = 181$, and (c) $N_\theta = 283$. The field scale is saturated at ± 15 G. Dash-dot line represents the sub-Earth positions.

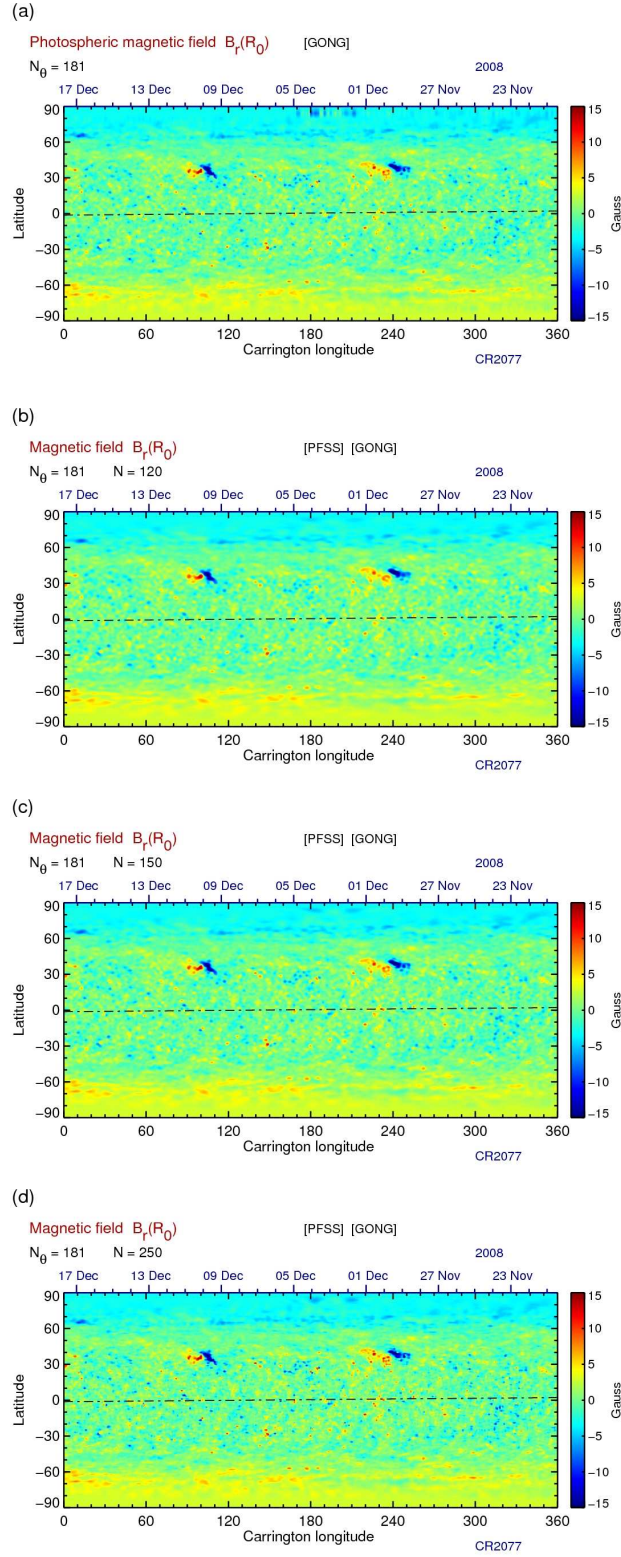


Figure 13: Magnetic field $B_r(R_0, \theta, \phi)$ from (a) the re-meshed CR2077 magnetogram, and from the PFSS model with (b) $N = 120$, (c) $N = 150$, and (d) $N = 250$. The number of grid points is $N_\theta = 181$ and $N_\phi = 360$. The field is saturated at ± 15 G. Dash-dot line represents the sub-Earth positions.

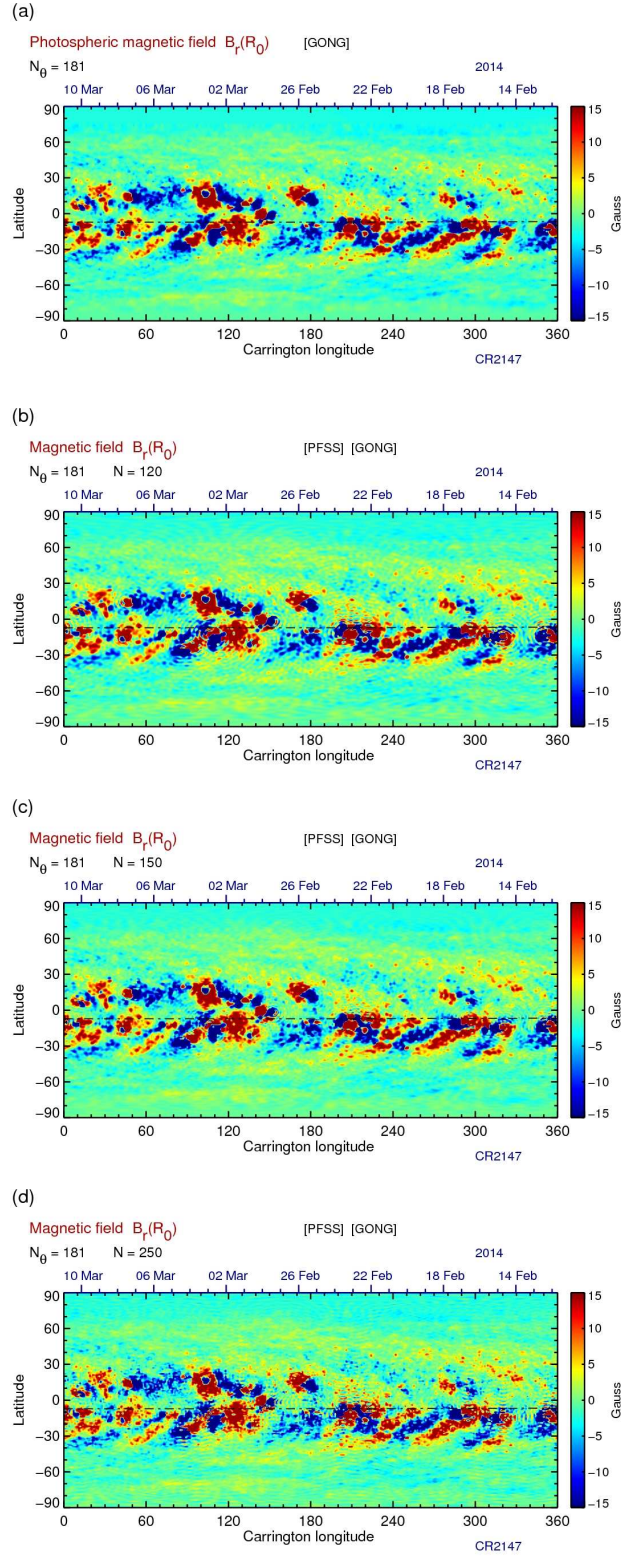


Figure 14: Magnetic field $B_r(R_0, \theta, \phi)$ from (a) the re-meshed CR2147 magnetogram, and from the PFSS model with (b) $N = 120$, (c) $N = 150$, and (d) $N = 250$. The number of grid points is $N_\theta = 181$ and $N_\phi = 360$. The field is saturated at ± 15 G. Dash-dot line represents the sub-Earth positions.

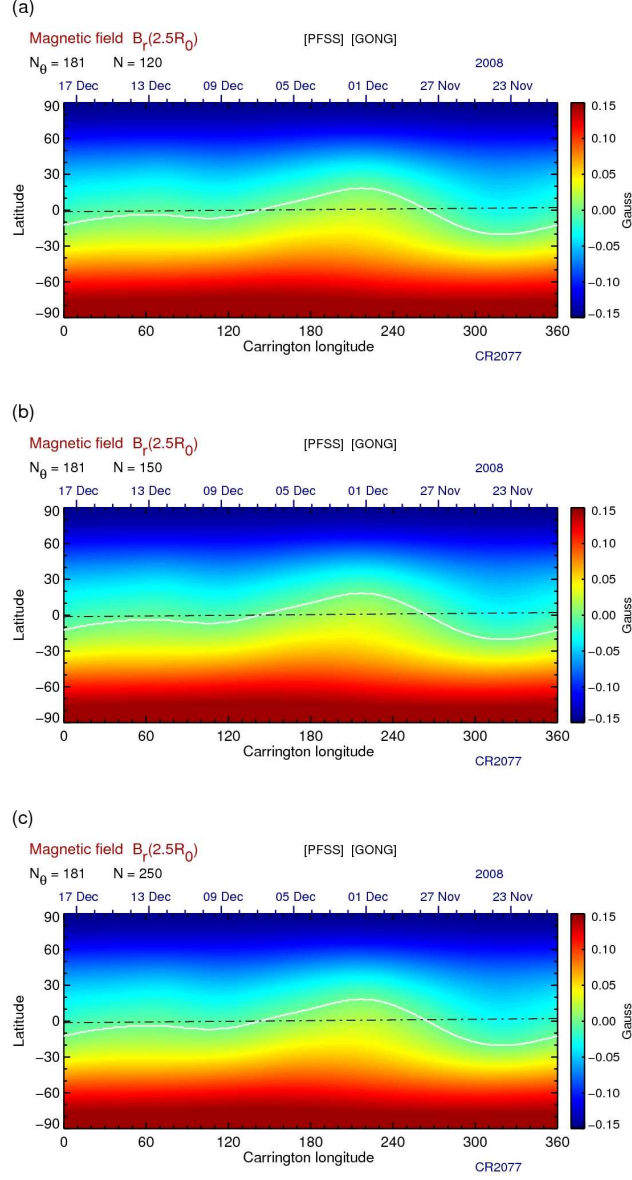


Figure 15: Magnetic field at the source-surface $B_r(2.5R_0, \theta, \phi)$ from the PFSS model for the re-meshed CR2077 magnetogram with $N_\theta = 181$ and $N_\phi = 360$. (a) $N = 120$, (b) $N = 150$, and (c) $N = 250$. The field is saturated at ± 0.15 G. White line represents the neutral line and dash-dot line denotes the sub-Earth positions.

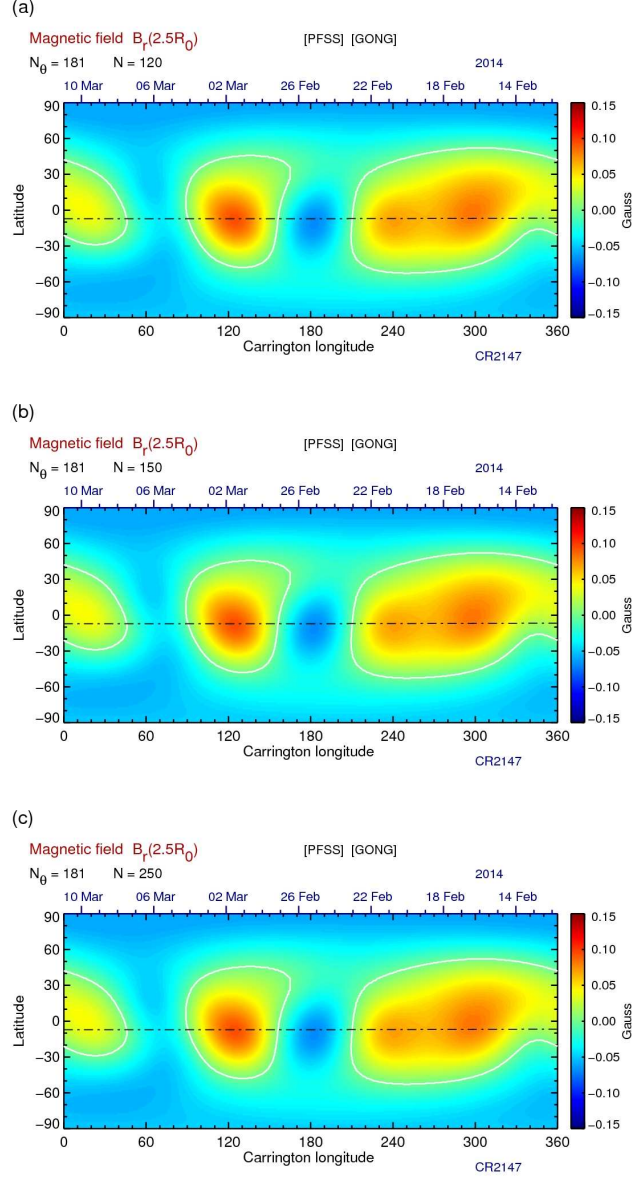


Figure 16: Magnetic field at the source-surface $B_r(2.5R_0, \theta, \phi)$ from the PFSS model for the re-meshed CR2147 magnetogram with $N_\theta = 181$ and $N_\phi = 360$. (a) $N = 120$, (b) $N = 150$, and (c) $N = 250$. The field is saturated at ± 0.15 G. White line represents the neutral line and dash-dot line denotes the sub-Earth positions.

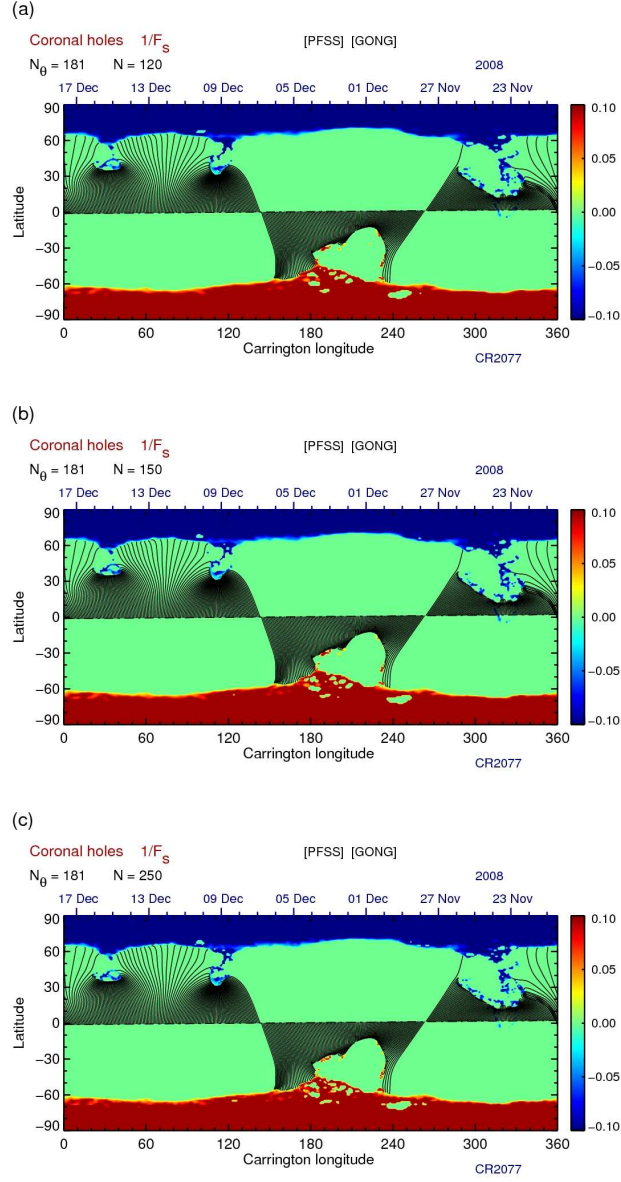


Figure 17: Derived COHO from the PFSS model for the re-meshed CR2077 magnetogram with $N_\theta = 181$ and $N_\phi = 360$. (a) $N = 120$, (b) $N = 150$, and (c) $N = 250$. $1/F_s$ is saturated at ± 0.1 . The black lines represent open magnetic field lines which connect the sub-Earth positions with COHO.

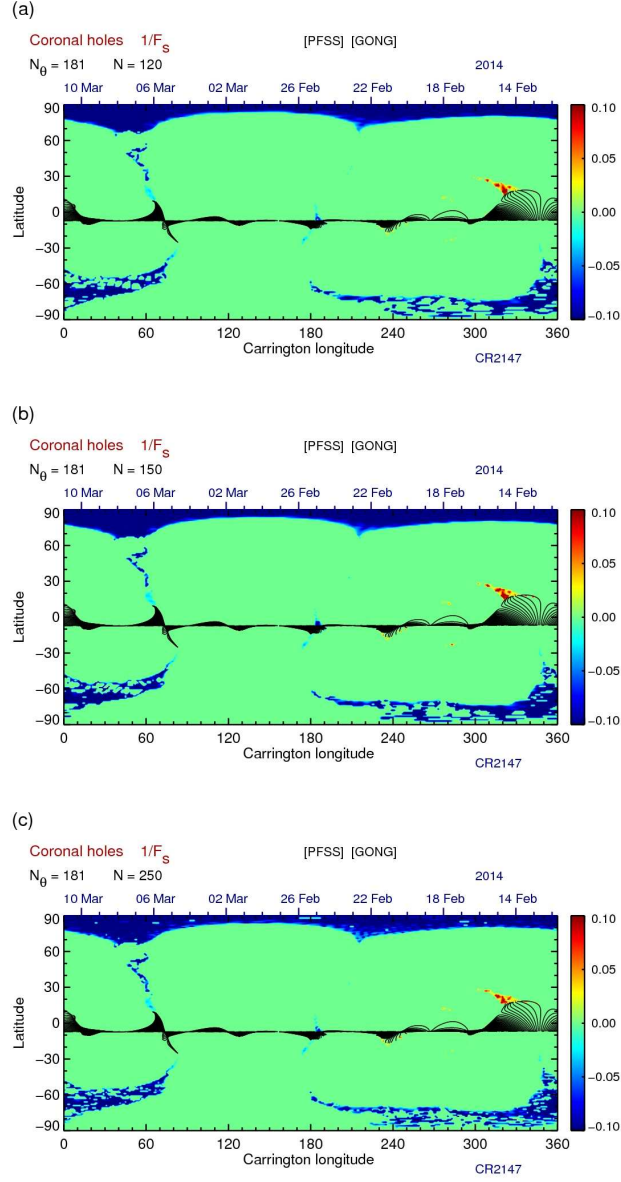


Figure 18: Derived COHO from the PFSS model for the re-meshed CR2147 magnetogram with $N_\theta = 181$ and $N_\phi = 360$. (a) $N = 120$, (b) $N = 150$, and (c) $N = 250$. $1/F_s$ is saturated at ± 0.1 . The black lines represent open magnetic field lines which connect the sub-Earth positions with COHO.

4.3 Angular resolution

The results in Fig. 13-18 are obtained with the PFSS model $1^\circ \times 1^\circ$ angular $\theta - \phi$ resolution. 1° corresponds to less than 2h in the Sun's 27-day rotation. Although high-resolution magnetograms and numerical models are in general desirable, from the practical point of view it is not always necessary to work with a high resolution model. In particular, when the uncertainty of models is greater than the benefit of using the high resolution.

In Fig. 19-24 we compare the results obtained using the re-meshed magnetograms with $N_\theta = 181$ and $N_\phi = 360$, and with the PFSS model angular resolution (a) $\Delta\theta = \Delta\phi = 1^\circ$ and (b) $\Delta\theta = \Delta\phi = 2.5^\circ$. In Fig. 19 and 20, we can see the results for $B_r(R_0, \theta, \phi)$ obtained with the CR2077 and CR2147 re-meshed magnetograms, respectively. With the lower resolution the fine details, including the ringing effect, are smoothed out. The difference $|\Phi^{1^\circ}(R_0) - \Phi^{2.5^\circ}(R_0)|/\Phi^{1^\circ}(R_0)$ in the unsigned magnetic fluxes between the cases with $\Delta\theta = \Delta\phi = 1^\circ$ and $\Delta\theta = \Delta\phi = 2.5^\circ$ are less than 1% for both, the CR2077 and CR2147 magnetogram.

At the source-surface, Fig. 21 and 22, the difference in unsigned magnetic fluxes between the cases with (a) $\Delta\theta = \Delta\phi = 1^\circ$ and (b) $\Delta\theta = \Delta\phi = 2.5^\circ$ is negligible. As we can see from Fig. 21 (CR2077) and 22 (CR2147) no visible differences are present.

As can be expected, due to the change in the resolution, the derived COHO shown in Fig. 23 (CR2077) and 24 (CR2147) for (a) $\Delta\theta = \Delta\phi = 1^\circ$ and (b) $\Delta\theta = \Delta\phi = 2.5^\circ$, show small differences. However, the topology of open magnetic field lines that connect with the sub-Earth positions is well preserved.

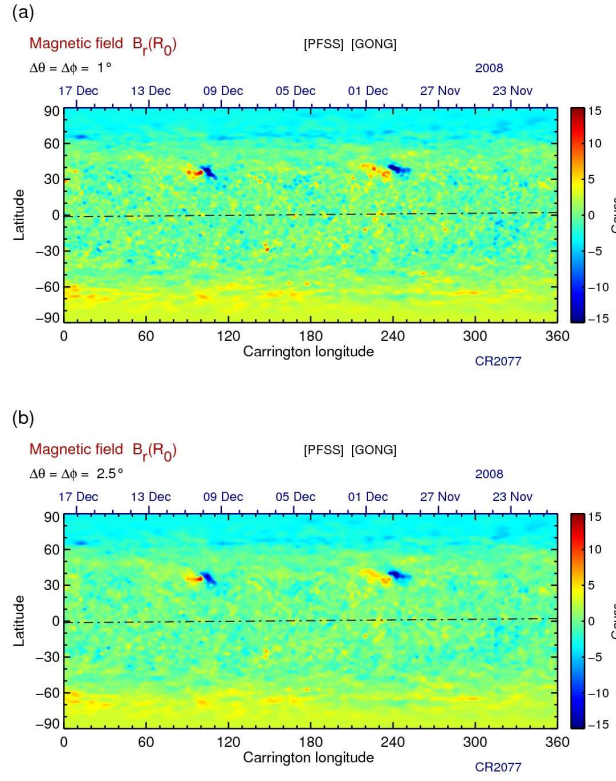


Figure 19: Magnetic field $B_r(R_0, \theta, \phi)$ from the PFSS model for the re-meshed CR2077 magnetogram with $N_\theta = 181$, $N_\phi = 360$, and $N = 120$. The angular resolution of the PFSS model is (a) $1^\circ \times 1^\circ$, and (b) $2.5^\circ \times 2.5^\circ$. The field is saturated at ± 15 G. Dash-dot line represents the sub-Earth positions.

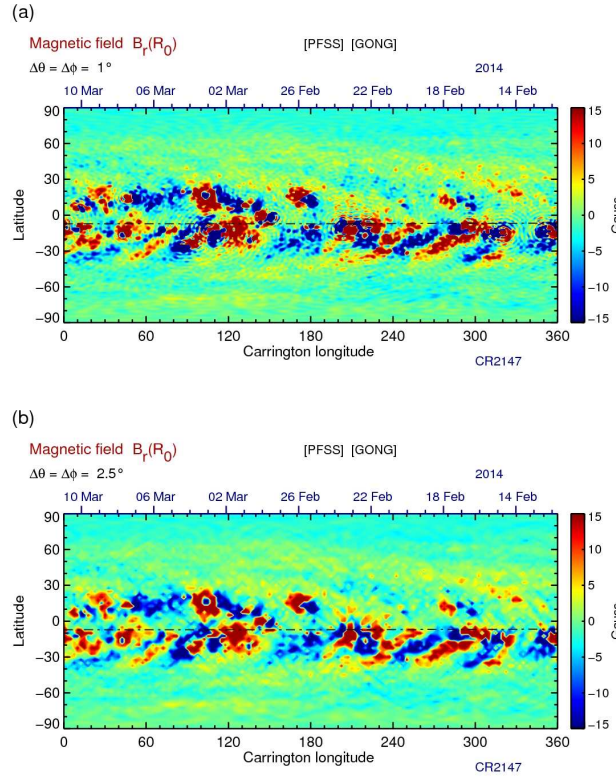


Figure 20: Magnetic field $B_r(R_0, \theta, \phi)$ from the PFSS model for the re-meshed CR2147 magnetogram with $N_\theta = 181$, $N_\phi = 360$, and $N = 120$. The angular resolution of the PFSS model is (a) $1^\circ \times 1^\circ$, and (b) $2.5^\circ \times 2.5^\circ$. The field is saturated at ± 15 G. Dash-dot line represents the sub-Earth positions.

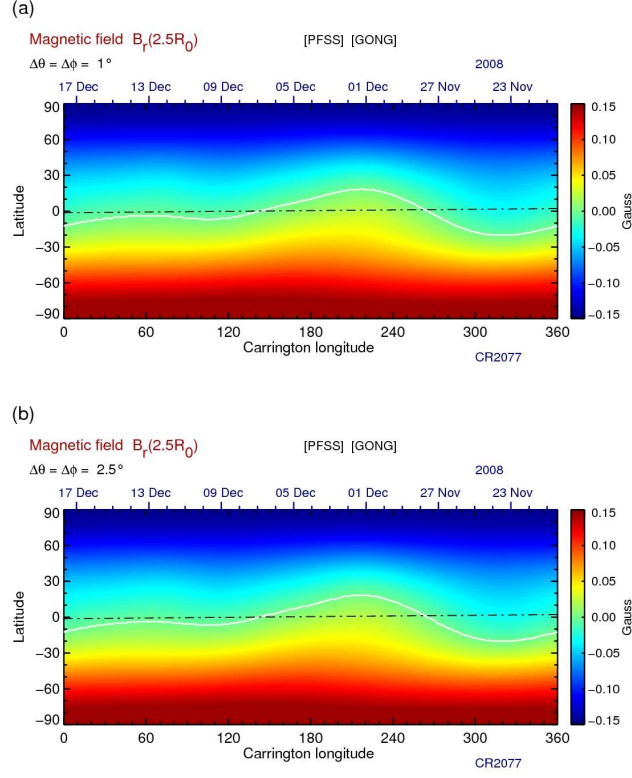


Figure 21: Magnetic field at the source-surface $B_r(2.5R_0, \theta, \phi)$ from the PFSS model for the re-meshed CR2077 magnetogram with $N_\theta = 181$, $N_\phi = 360$, and $N = 120$. The angular resolution of the PFSS model is (a) $1^\circ \times 1^\circ$, and (b) $2.5^\circ \times 2.5^\circ$. The field is saturated at ± 0.15 G. White line represents the neutral line and dash-dot line denotes the sub-Earth positions.

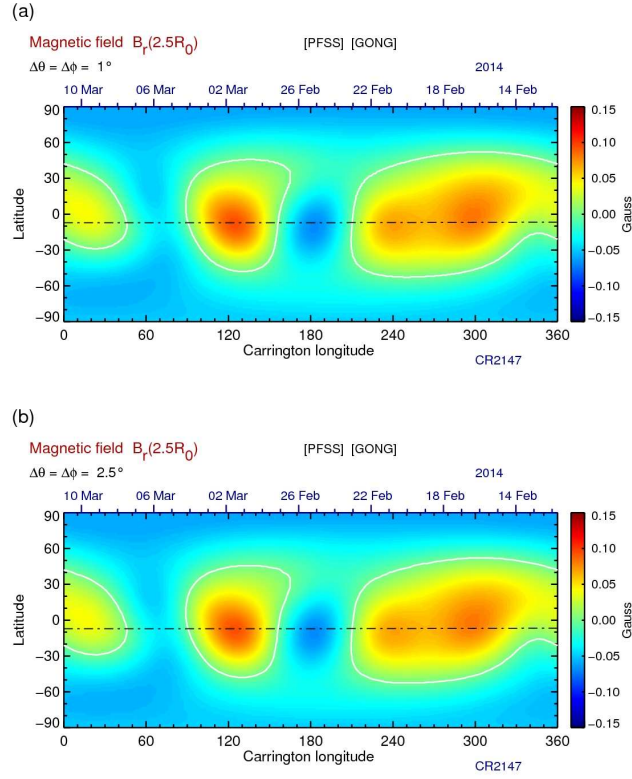


Figure 22: Magnetic field at the source-surface $B_r(2.5R_0, \theta, \phi)$ from the PFSS model for the re-meshed CR2147 magnetogram with $N_\theta = 181$, $N_\phi = 360$, and $N = 120$. The angular resolution of the PFSS model is (a) $1^\circ \times 1^\circ$, and (b) $2.5^\circ \times 2.5^\circ$. The field is saturated at ± 0.15 G. White line represents the neutral line and dash-dot line denotes the sub-Earth positions.

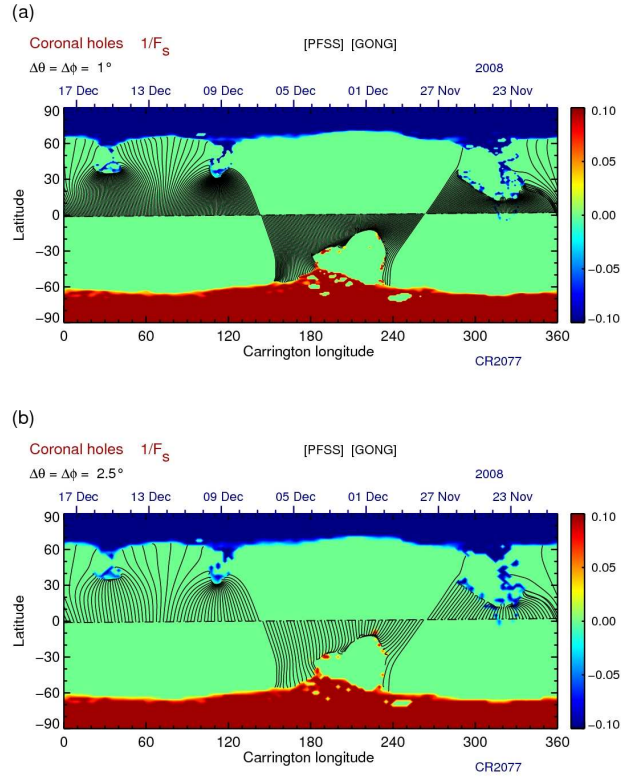


Figure 23: Derived COHO from the PFSS model for the re-meshed CR277 magnetogram with $N_\theta = 181$, $N_\phi = 360$, and $N = 120$. The angular resolution of the PFSS model is (a) $1^\circ \times 1^\circ$, and (b) $2.5^\circ \times 2.5^\circ$. $1/F_s$ is saturated at ± 0.1 . The black lines represent open magnetic field lines which connect the sub-Earth positions with COHO.

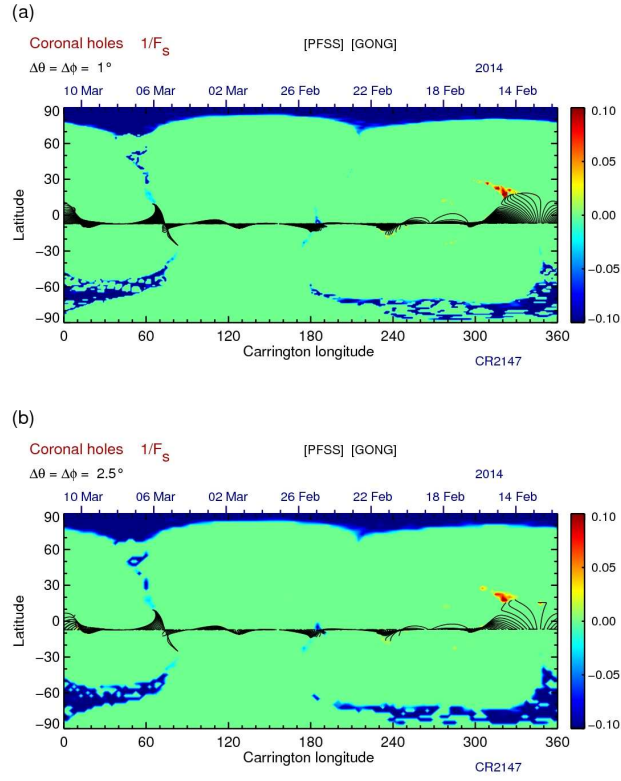


Figure 24: Derived COHO from the PFSS model for the re-meshed CR2077 magnetogram with $N_\theta = 181$, $N_\phi = 360$, and $N = 120$. The angular resolution of the PFSS model is (a) $1^\circ \times 1^\circ$, and (b) $2.5^\circ \times 2.5^\circ$. $1/F_s$ is saturated at ± 0.1 . The black lines represent open magnetic field lines which connect the sub-Earth positions with COHO.

4.4 Schatten model - principal index N_s

The previous results are obtained by the PFSS model which covers the $R_0 \leq r \leq R_s$ coronal field region. To extend the field beyond R_s , we will include the SCS model here. Similar to the WSA model, we place the cusp surface at the same location as the source-surface, $R_{cp} = R_s = 2.5R_0$, and investigate how the solutions depend on the principal index N_s used to match $r > R_{cp}$ solutions Eq. (53)-(55) with the PFSS solutions Eq. (42)-(44) at R_s .

In Fig. 25-26 we can see the SCS solutions for the magnetic field $B_r(5R_0, \theta, \phi)$ at $r = 5R_0$. These results are obtained by matching the field to the PFSS solutions at $R_s = 2.5R_0$ using (a) $N_s = 10$, (b) $N_s = 20$, and (c) $N_s = 30$, for CR2077 (Fig. 25) and CR2147 (Fig. 26). The angular resolution used in the models is $2.5^\circ \times 2.5^\circ$, and the degree of harmonics used in the PFSS model is limited to $N = 120$. The re-meshed magnetograms are obtained with $N_\theta = 181$ and $N_\phi = 360$. The difference between unsigned magnetic fluxes obtained by the SCS model for $N_s = 10$, $N_s = 20$, and $N_s = 30$ at $5R_0$ is negligible for both the CR2077 and CR2147 case. The difference in unsigned magnetic fluxes obtained by the PFSS model $\Phi^P(R_s)$ at $R_s = 2.5R_0$, and the SCS model $\Phi^{Sh}(R_s)$ at $5R_0$ using $N_s = 10$, i.e. $|\Phi^P(2.5R_0) - \Phi^{Sh}(5R_0)|/\Phi^P(R_0)$, is $\approx 12\%$ and $\approx 2\%$ for CR2077 and CR2147, respectively.

We conclude that using $N_s = 10$ in the SCS model is sufficient to obtain a good solution. This is also confirmed by Fig. 27-28 where we show derived COHO and open magnetic field lines which connect to the sub-Earth locations for CR2077 (Fig. 27) and CR2147 (Fig. 28), respectively. The parameters are the same as in the case of Fig. 25-26. As we can see, there are no noticeable differences between cases (a) $N_s = 10$, (b) $N_s = 20$, and (c) $N_s = 30$.

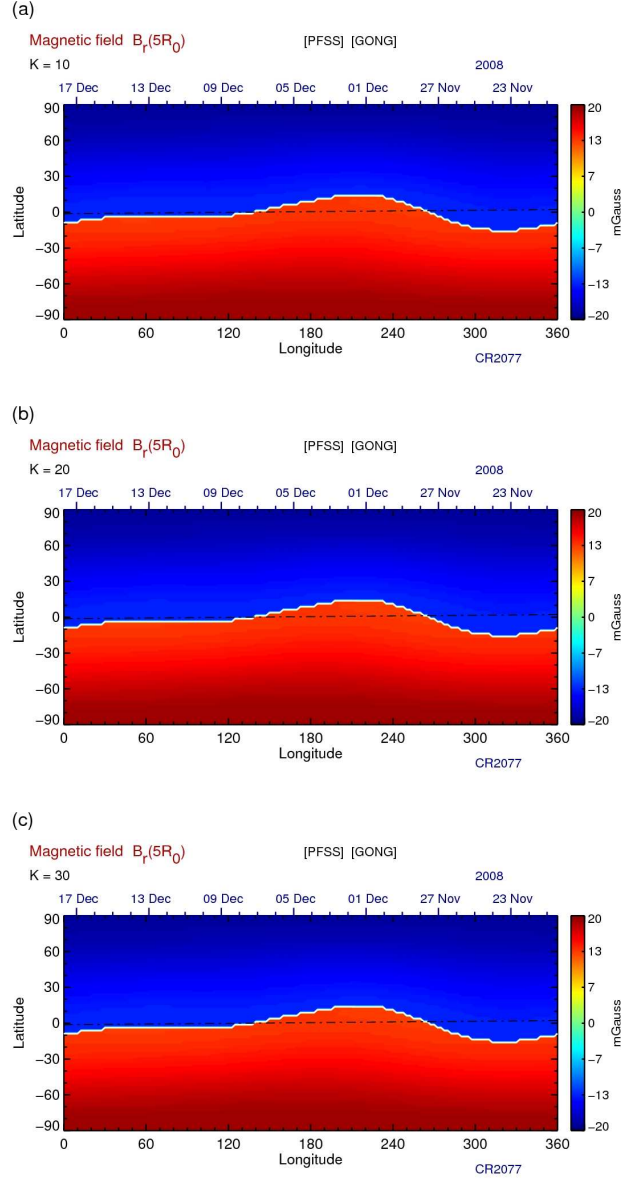


Figure 25: Magnetic field $B_r(5R_0, \theta, \phi)$ for the re-meshed ($N_\theta = 181$, $N_\phi = 360$) CR2077 magnetogram from the PFSS-SCS model with (a) $N_s = 10$, (b) $N_s = 20$, and (c) $N_s = 30$. The field is saturated at ± 0.2 mG. White line represents the neutral line and dash-dot line denotes the sub-Earth positions.

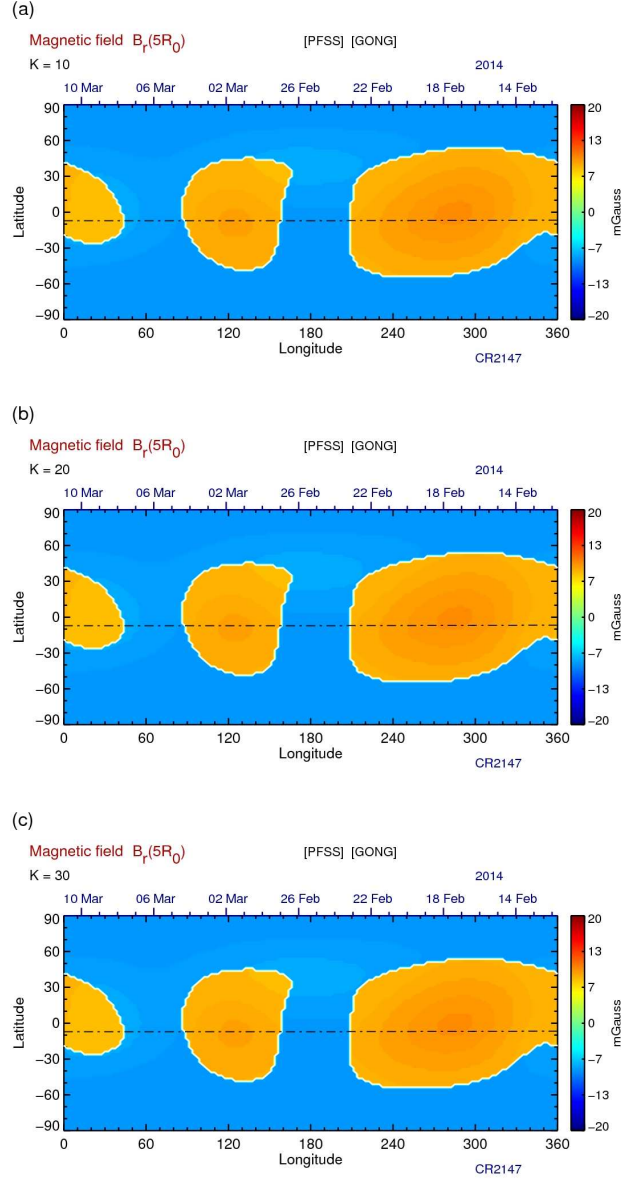


Figure 26: Magnetic field $B_r(5R_0, \theta, \phi)$ for the re-meshed ($N_\theta = 181$, $N_\phi = 360$) CR2147 magnetogram from the PFSS-SCS model with (a) $N_s = 10$, (b) $N_s = 20$, and (c) $N_s = 30$. The field is saturated at ± 0.2 mG. White line represents the neutral line and dash-dot line denotes the sub-Earth positions.

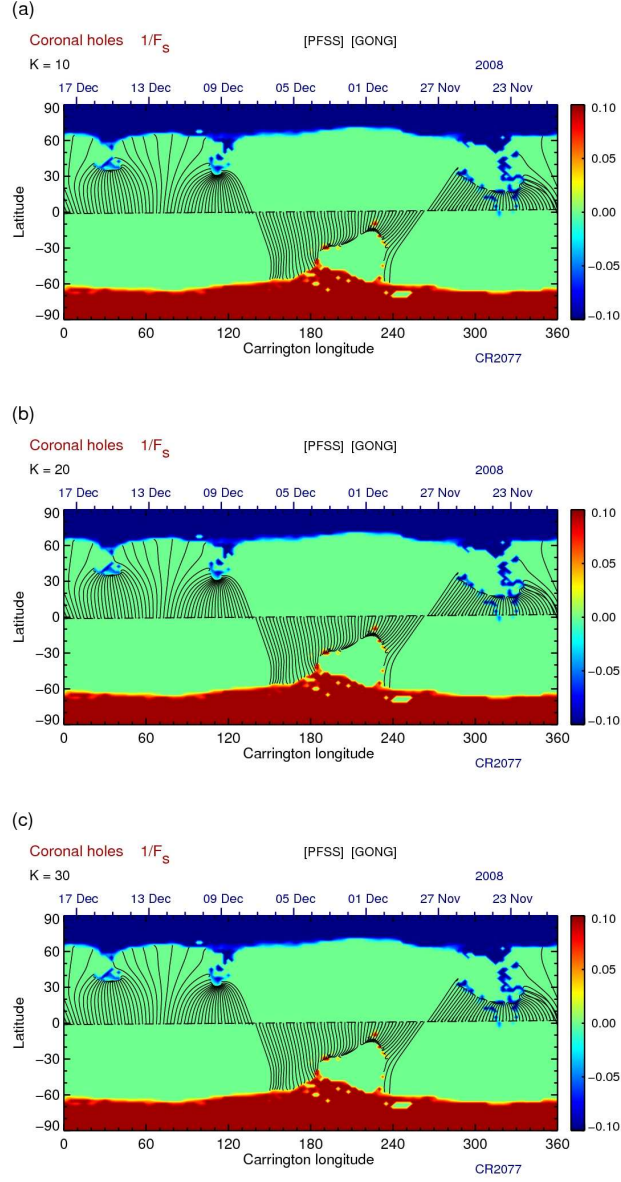


Figure 27: Derived COHO from the PFSS-SCS model for the re-meshed ($N_\theta = 181$, $N_\phi = 360$) CR2077 magnetogram with (a) $N_s = 10$, (b) $N_s = 20$, and (c) $N_s = 30$. $1/F_s$ is saturated at ± 0.1 . The black lines represent open magnetic field lines which connect the sub-Earth positions with COHO.

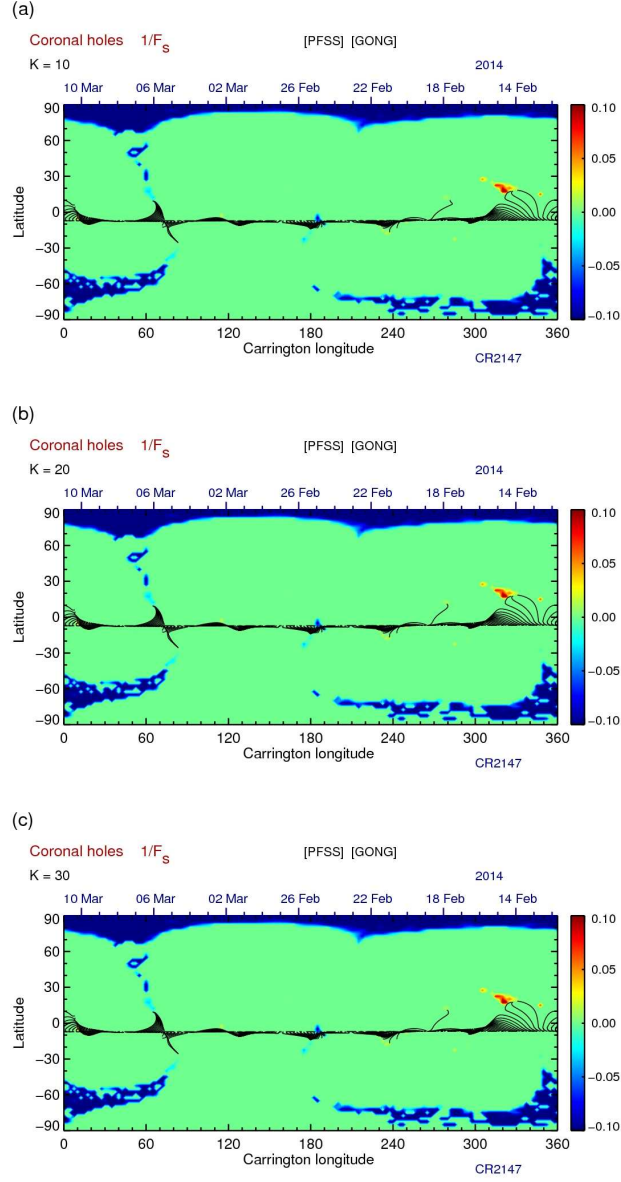


Figure 28: Derived COHO from the PFSS-SCS model for the re-meshed ($N_\theta = 181$, $N_\phi = 360$) CR2147 magnetogram with (a) $N_s = 10$, (b) $N_s = 20$, and (c) $N_s = 30$. $1/F_s$ is saturated at ± 0.1 . The black lines represent open magnetic field lines which connect the sub-Earth positions with COHO.

4.5 Radial resolution

We examined how the change in the angular resolution of the coronal field model impacts the results. Here we will briefly consider the radial step Δr used in the coupled PFSS-SCS model.

In Fig. 29 and 30, the derived COHO and open magnetic field lines which connect the sub-Earth positions for two choices of the radial step (a) $\Delta r = 0.01R_0$, and (b) $\Delta r = 0.02R_0$ for CR2077 (Fig. 29) and CR2147 (Fig. 30) are shown. The angular resolution is $\Delta\theta = \Delta\phi = 2.5^\circ$. $N_\theta = 181$ and $N_\phi = 360$ are used to obtain the re-meshed magnetograms. N in the PFSS model is set to 120, and in the SCS model we use $N_s = 20$. The coronal field lines are traced between the photosphere (R_0) and $5R_0$. As we can see, no differences in the derived COHO and field lines are found which justifies the choice of the radial step Δr used in numerical calculations.

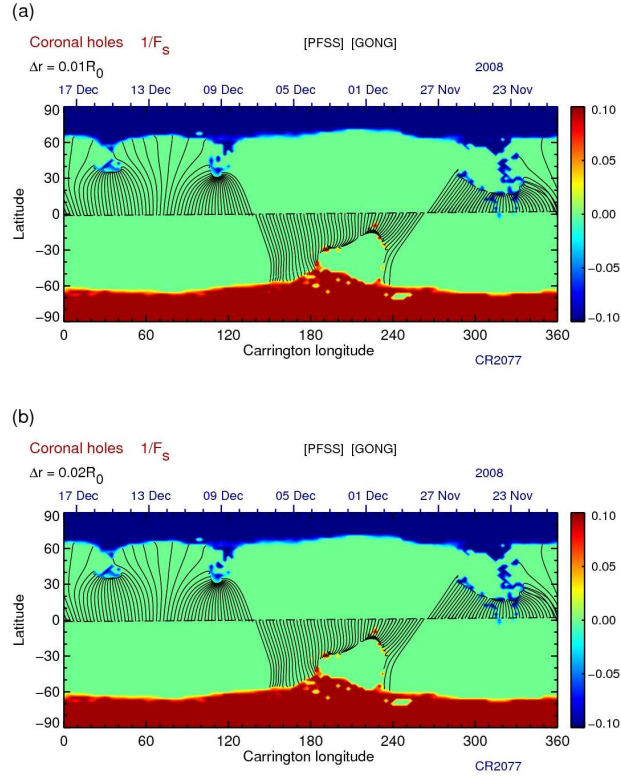


Figure 29: Derived COHO from the PFSS-SCS model for the re-meshed CR2077 magnetogram ($N_\theta = 181$, $N_\phi = 360$). The angular resolution is set to $\Delta\theta = \Delta\phi = 2.5^\circ$, and the radial step is (a) $\Delta r = 0.01R_0$, and (b) $\Delta r = 0.02R_0$. The PFSS model uses $N = 120$ and the SCS model uses $N_s = 20$. $1/F_s$ is saturated at ± 0.1 . The black lines represent open magnetic field lines which connect the sub-Earth positions with COHO.

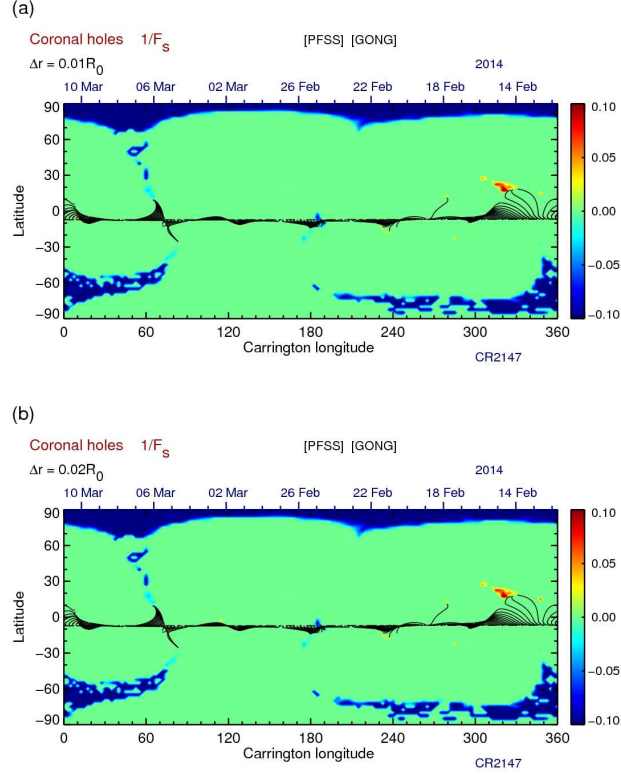


Figure 30: Derived COHO from the PFSS model for the re-meshed CR2147 magnetogram ($N_\theta = 181$, $N_\phi = 360$). The angular resolution is set to $\Delta\theta = \Delta\phi = 2.5^\circ$, and the radial step is (a) $\Delta r = 0.01R_0$, and (b) $\Delta r = 0.02R_0$. The PFSS model uses $N = 120$ and the SCS model uses $N_s = 20$. $1/F_s$ is saturated at ± 0.1 . The black lines represent open magnetic field lines which connect the sub-Earth positions with COHO.

4.6 Height of the source-surface

The previous numerical results mainly focus on numerical accuracy. However, the only parameter that is free in the PFSS equations for the coronal field Eq. (42)-(44) is the radius of the source-surface R_s . Although $R_s = 2.5R_0$ is widely used, this does not represent the best choice for the location of the source-surface for all periods of solar activity [35], [36].

To illustrate the changes introduced by different heights of the source-surface we show here the PFSS-SCS model outputs for the case with $R_s = 1.5R_0$ (Fig. 31-36), and the case with $R_s = 3.5R_0$ (Fig. 37-42). These figures can be compared with the previously obtained figures for $R_s = 2.5R_0$.

In Fig. 31-33, we can see the results for the radial component of the magnetic field at $R_s = 1.5R_0$ from the PFSS model (Fig. 31), the magnetic field $B_r(5R_0, \theta, \phi)$ at $5R_0$ from the SCS model (Fig. 32), and derived COHO and open magnetic field lines which connect the sub-Earth positions (Fig. 33). These figures are obtained with the re-meshed CR2077 magnetogram with $N = 120$, $N_s = 10$, $N_\phi = 360$, and (a) $N_\theta = 181$, $\Delta\theta = \Delta\phi = 2.5^\circ$, $\Delta r = 0.02R_0$; (b) $N_\theta = 283$, $\Delta\theta = \Delta\phi = 2.5^\circ$, $\Delta r = 0.01R_0$; (c) $N_\theta = 283$, $\Delta\theta = \Delta\phi = 1^\circ$, $\Delta r = 0.01R_0$.

The same representation of quantities and parameters as in Fig. 31-33, are used in Fig. 34-36 which are based on the re-meshed CR2147 magnetogram.

Figures 37-42 are obtained with $R_s = 3.5R_0$. The choice of other parameters in Fig. 37-39 (CR2077) and Fig. 40-42 (CR2147) is the same as in Fig. 31-33 (CR2077) and Fig. 34-36 (CR2147).

Comparison of the corresponding figures for $R_s = 1.5R_0$, $R_s = 2.5R_0$ and $R_s = 3.5R_0$ reveals significant differences. The location of the neutral line, magnetic field intensity and the size and location of the derived COHO are significantly altered by changing location of the source-surface. The difference in unsigned magnetic fluxes at $5R_0$ for CR2044, for example, for the cases from Fig. 25a ($R_s = 2.5R_0$), and Fig. 32a ($R_s = 1.5R_0$), and Fig. 38a ($R_s = 3.5R_0$), i.e. $|\Phi^{2.5}(5R_0) - \Phi^{1.5}(5R_0)|/\Phi^{2.5}(5R_0)$ and $|\Phi^{2.5}(5R_0) - \Phi^{3.5}(5R_0)|/\Phi^{2.5}(5R_0)$, is $\approx 56\%$ and $\approx 27\%$, respectively. As is expected, with decreasing the height of the source-surface, the unsigned magnetic flux associated with open magnetic field lines increases, $\Phi^{1.5}(5R_0) > \Phi^{2.5}(5R_0) > \Phi^{3.5}(5R_0)$.

The same calculations for the CR2147 magnetogram based on results from Fig. 26a ($R_s = 2.5R_0$), and Fig. 35a ($R_s = 1.5R_0$), and Fig. 41a ($R_s = 3.5R_0$) show $\approx 253\%$ and $\approx 51\%$ difference in the unsigned magnetic fluxes.

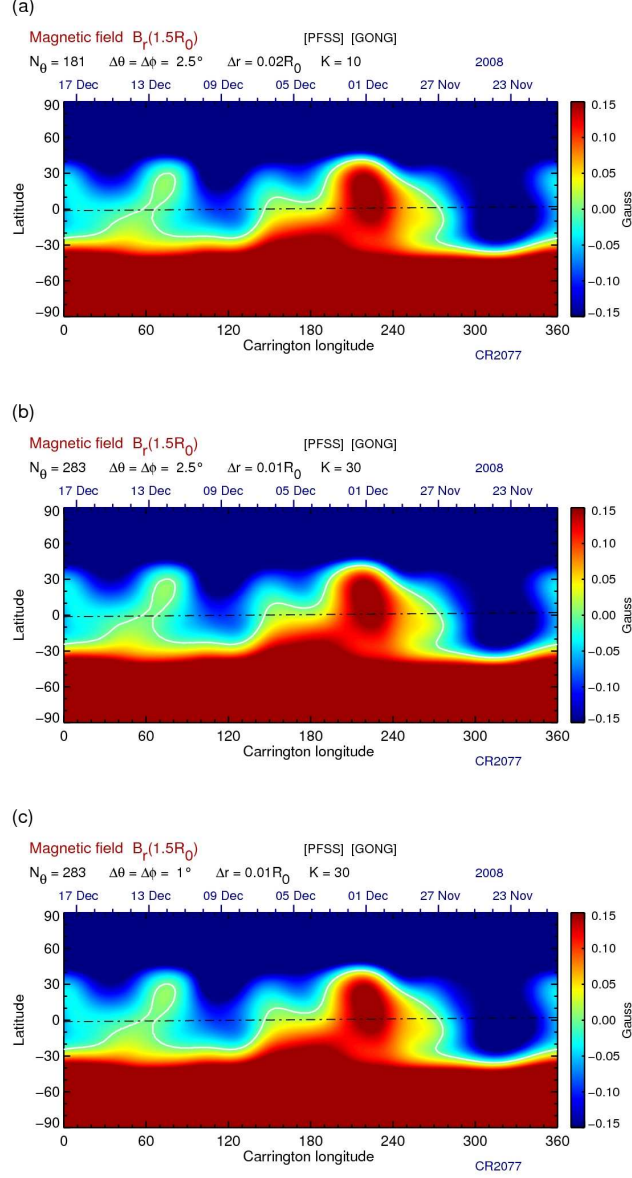


Figure 31: Magnetic field at the source-surface $B_r(1.5R_0, \theta, \phi)$ from the PFSS model for the re-meshed CR2077 magnetogram. The parameters are $R_s = 1.5R_0$, $N = 120$, $N_s = 10$, $N_\phi = 360$, and (a) $N_\theta = 181$, $\Delta\theta = \Delta\phi = 2.5^\circ$, $\Delta r = 0.02R_0$, (b) $N_\theta = 283$, $\Delta\theta = \Delta\phi = 2.5^\circ$, $\Delta r = 0.01R_0$, (c) $N_\theta = 283$, $\Delta\theta = \Delta\phi = 1^\circ$, $\Delta r = 0.01R_0$. The field is saturated at ± 0.15 G. White line represents the neutral line and dash-dot line denotes the sub-Earth positions.

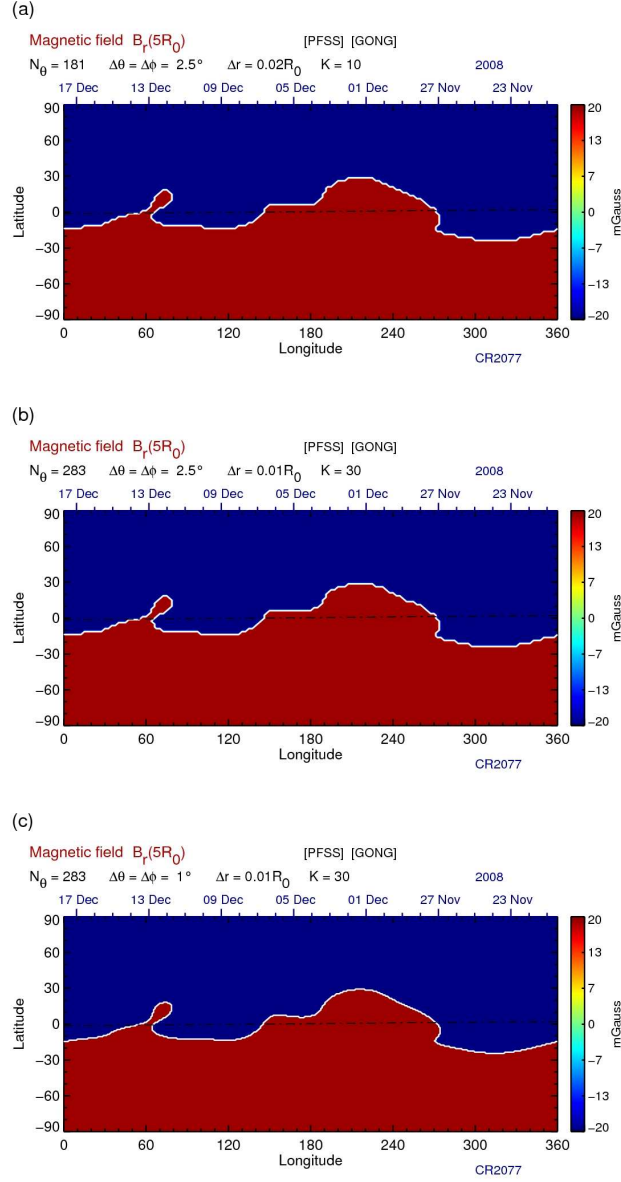


Figure 32: Magnetic field $B_r(5R_0, \theta, \phi)$ from the SCS model for the re-meshed CR2077 magnetogram. The parameters are $R_s = 1.5R_0$, $N = 120$, $N_s = 10$, $N_\phi = 360$, and (a) $N_\theta = 181$, $\Delta\theta = \Delta\phi = 2.5^\circ$, $\Delta r = 0.02R_0$, (b) $N_\theta = 283$, $\Delta\theta = \Delta\phi = 2.5^\circ$, $\Delta r = 0.01R_0$, (c) $N_\theta = 283$, $\Delta\theta = \Delta\phi = 1^\circ$, $\Delta r = 0.01R_0$. The field is saturated at ± 0.2 mG. White line represents the neutral line and dash-dot line denotes the sub-Earth positions.

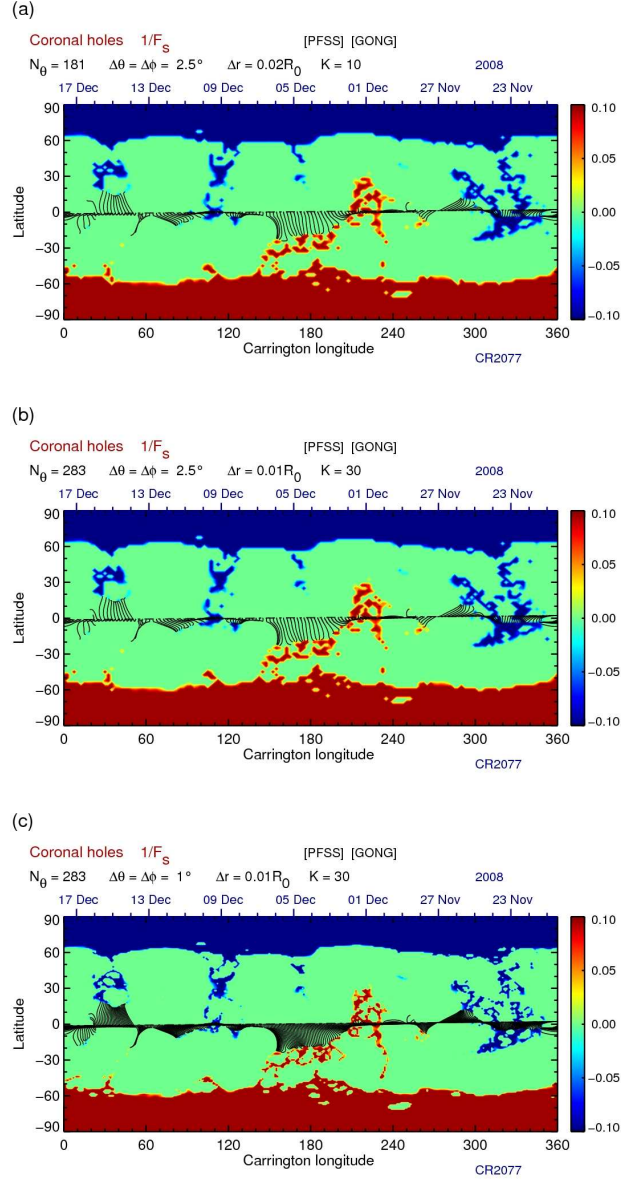


Figure 33: Derived COHO from the PFSS-SCS model for the re-meshed CR2077 magnetogram. The parameters are $R_s = 1.5R_0$, $N = 120$, $N_s = 10$, $N_\phi = 360$, and (a) $N_\theta = 181$, $\Delta\theta = \Delta\phi = 2.5^\circ$, $\Delta r = 0.02R_0$, (b) $N_\theta = 283$, $\Delta\theta = \Delta\phi = 2.5^\circ$, $\Delta r = 0.01R_0$, (c) $N_\theta = 283$, $\Delta\theta = \Delta\phi = 1^\circ$, $\Delta r = 0.01R_0$. $1/F_s$ is saturated at ± 0.1 . The black lines represent open magnetic field lines which connect the sub-Earth positions with COHO.

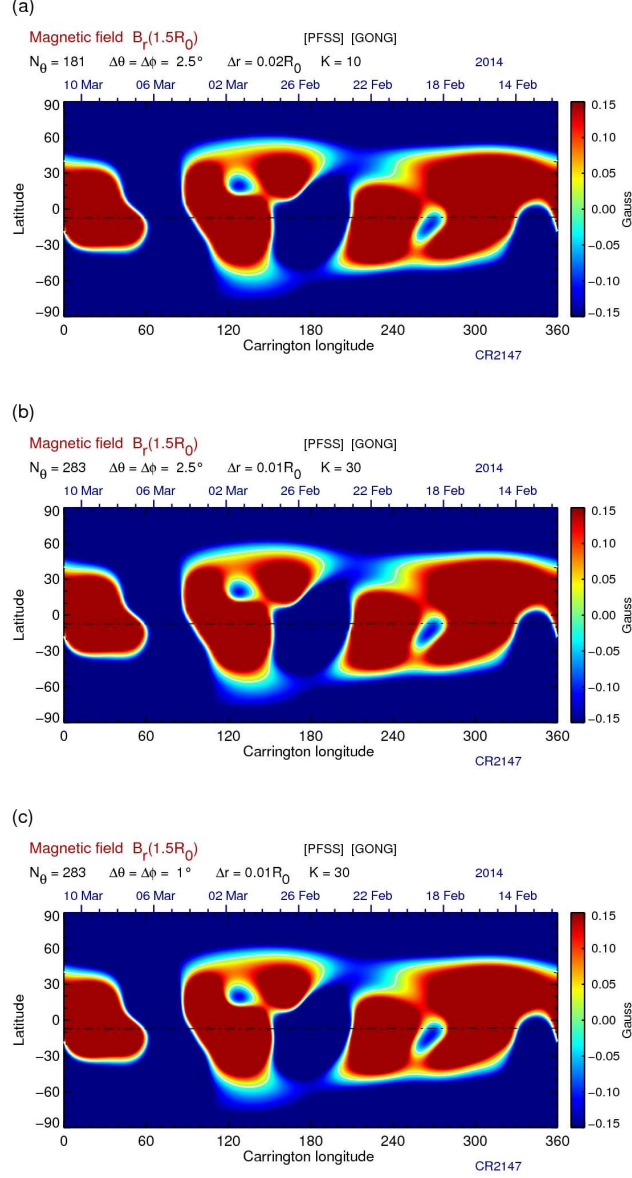


Figure 34: Magnetic field at the source-surface $B_r(1.5R_0, \theta, \phi)$ from the PFSS model for the re-meshed CR2147 magnetogram. The parameters are $R_s = 1.5R_0$, $N = 120$, $N_s = 10$, $N_\phi = 360$, and (a) $N_\theta = 181$, $\Delta\theta = \Delta\phi = 2.5^\circ$, $\Delta r = 0.02R_0$, (b) $N_\theta = 283$, $\Delta\theta = \Delta\phi = 2.5^\circ$, $\Delta r = 0.01R_0$, (c) $N_\theta = 283$, $\Delta\theta = \Delta\phi = 1^\circ$, $\Delta r = 0.01R_0$. The field is saturated at ± 0.15 G. White line represents the neutral line and dash-dot line denotes the sub-Earth positions.

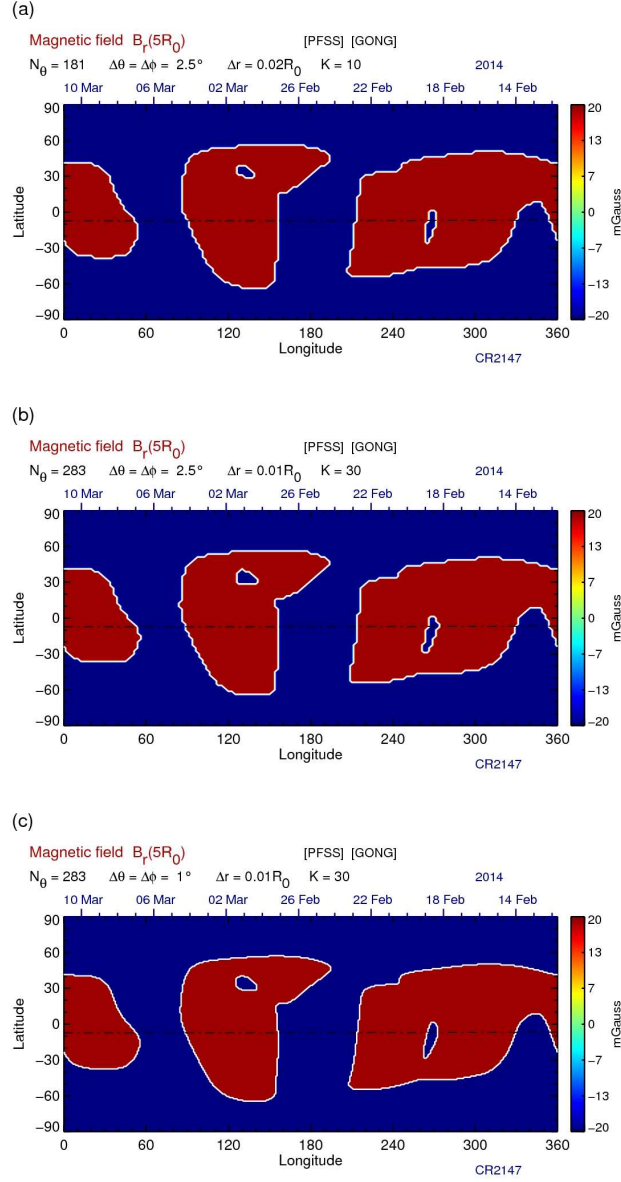


Figure 35: Magnetic field $B_r(5R_0, \theta, \phi)$ from the SCS model for the re-meshed CR2147 magnetogram. The parameters are $R_s = 1.5R_0$, $N = 120$, $N_s = 10$, $N_\phi = 360$, and (a) $N_\theta = 181$, $\Delta\theta = \Delta\phi = 2.5^\circ$, $\Delta r = 0.02R_0$, (b) $N_\theta = 283$, $\Delta\theta = \Delta\phi = 2.5^\circ$, $\Delta r = 0.01R_0$, (c) $N_\theta = 283$, $\Delta\theta = \Delta\phi = 1^\circ$, $\Delta r = 0.01R_0$. The field is saturated at ± 0.2 mG. White line represents the neutral line and dash-dot line denotes the sub-Earth positions.

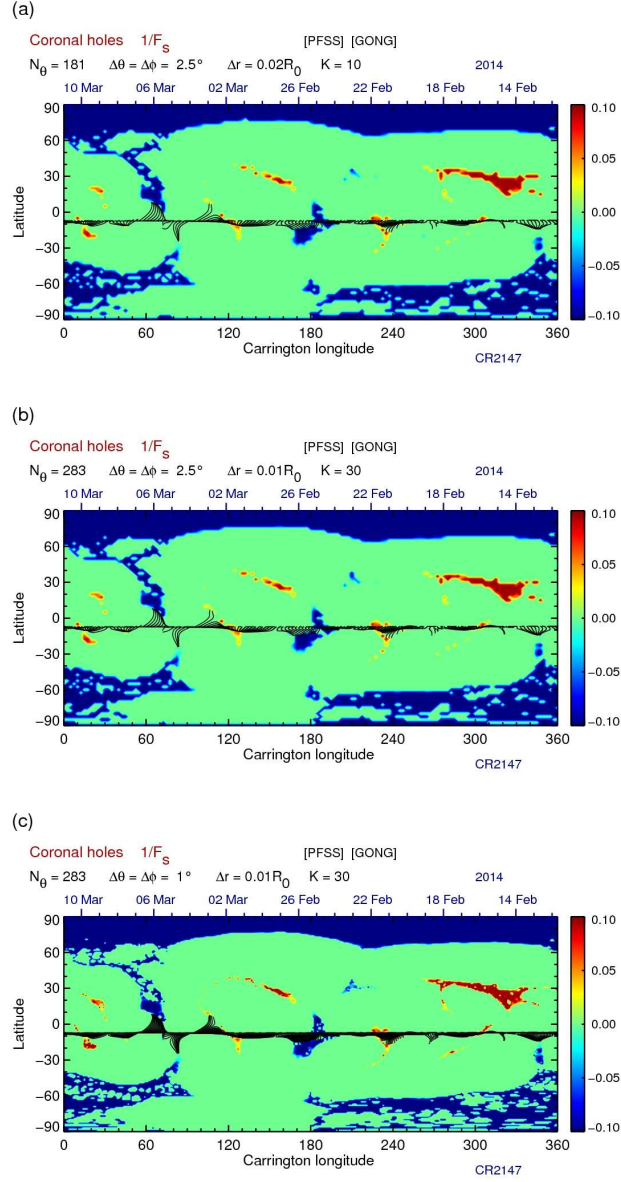


Figure 36: Derived COHO from the PFSS-SCS model for the re-meshed CR2147 magnetogram. The parameters are $R_s = 1.5R_0$, $N = 120$, $N_s = 10$, $N_\phi = 360$, and (a) $N_\theta = 181$, $\Delta\theta = \Delta\phi = 2.5^\circ$, $\Delta r = 0.02R_0$, (b) $N_\theta = 283$, $\Delta\theta = \Delta\phi = 2.5^\circ$, $\Delta r = 0.01R_0$, (c) $N_\theta = 283$, $\Delta\theta = \Delta\phi = 1^\circ$, $\Delta r = 0.01R_0$. $1/F_s$ is saturated at ± 0.1 . The black lines represent open magnetic field lines which connect the sub-Earth positions with COHO.

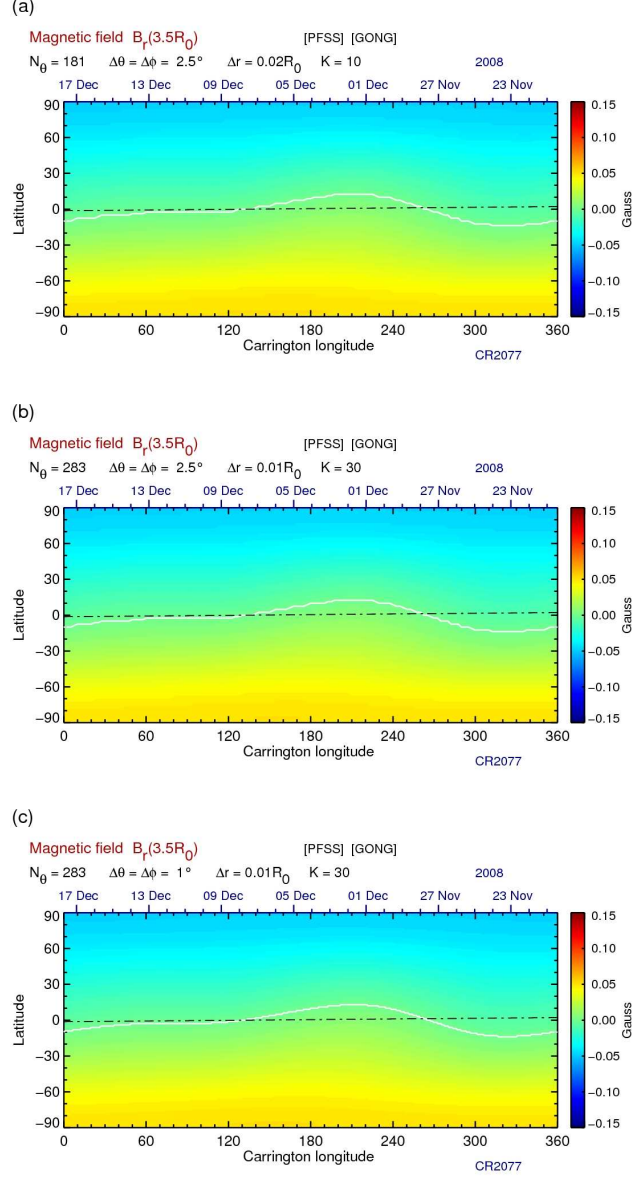


Figure 37: Magnetic field at the source-surface $B_r(1.5R_0, \theta, \phi)$ from the PFSS model for the re-meshed CR2077 magnetogram. The parameters are $R_s = 3.5R_0$, $N = 120$, $N_s = 10$, $N_\phi = 360$, and (a) $N_\theta = 181$, $\Delta\theta = \Delta\phi = 2.5^\circ$, $\Delta r = 0.02R_0$, (b) $N_\theta = 283$, $\Delta\theta = \Delta\phi = 2.5^\circ$, $\Delta r = 0.01R_0$, (c) $N_\theta = 283$, $\Delta\theta = \Delta\phi = 1^\circ$, $\Delta r = 0.01R_0$. The field is saturated at ± 0.15 G. White line represents the neutral line and dash-dot line denotes the sub-Earth positions.

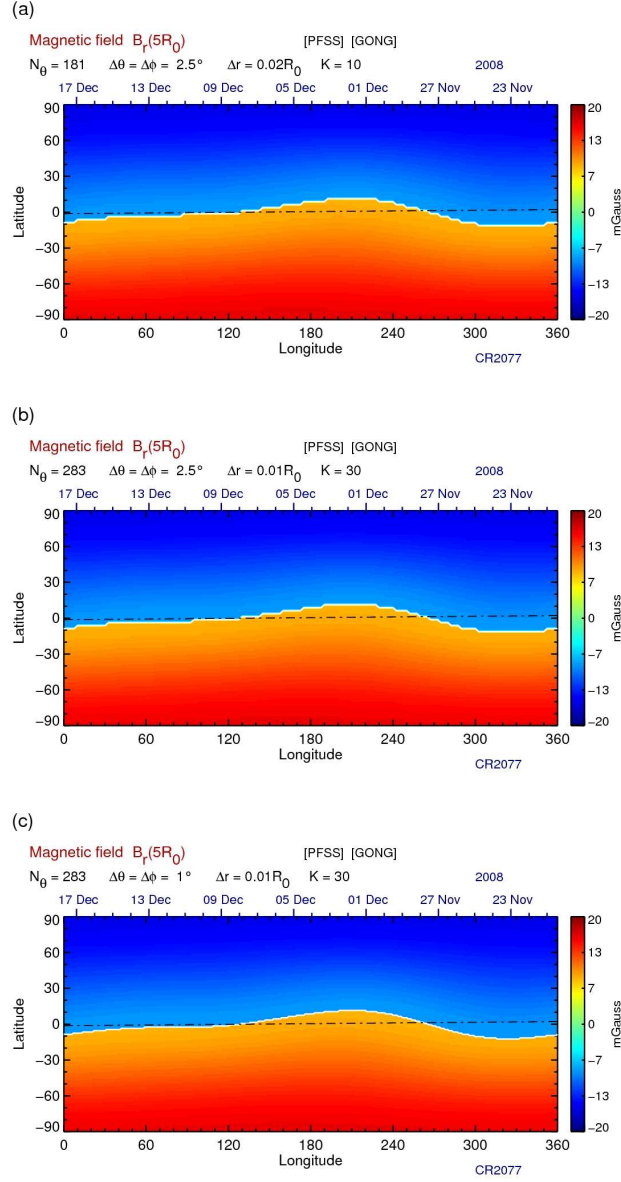


Figure 38: Magnetic field $B_r(5R_0, \theta, \phi)$ from the SCS model for the re-meshed CR2077 magnetogram. The parameters are $R_s = 3.5R_0$, $N = 120$, $N_s = 10$, $N_\phi = 360$, and (a) $N_\theta = 181$, $\Delta\theta = \Delta\phi = 2.5^\circ$, $\Delta r = 0.02R_0$, (b) $N_\theta = 283$, $\Delta\theta = \Delta\phi = 2.5^\circ$, $\Delta r = 0.01R_0$, (c) $N_\theta = 283$, $\Delta\theta = \Delta\phi = 1^\circ$, $\Delta r = 0.01R_0$. The field is saturated at ± 0.2 mG. White line represents the neutral line and dash-dot line denotes the sub-Earth positions.

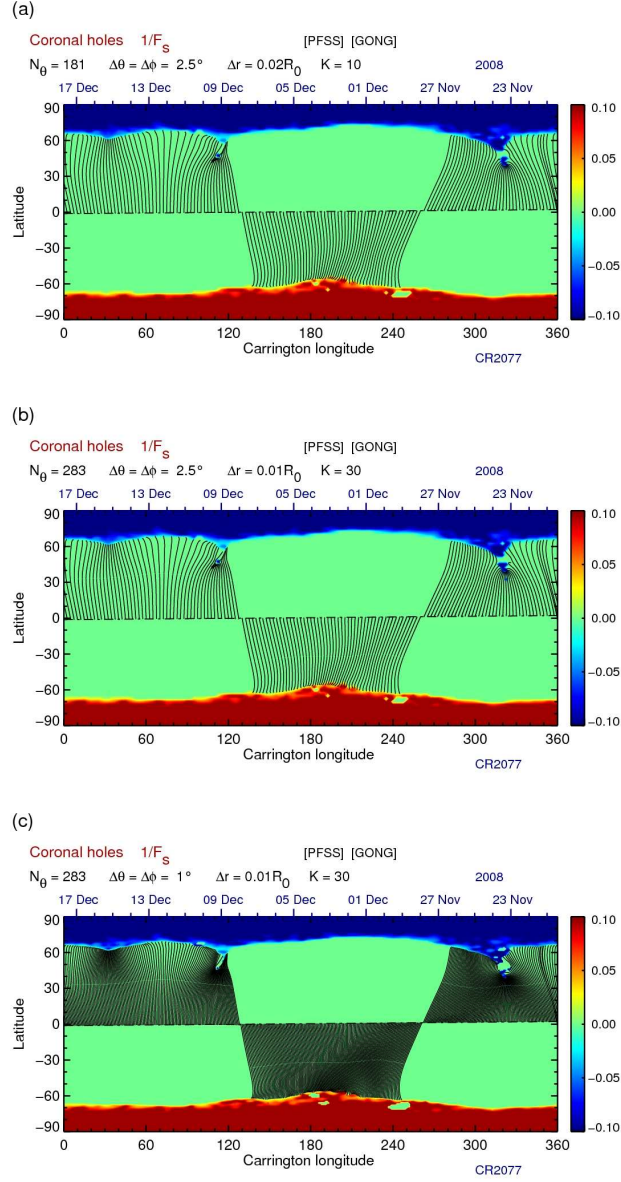


Figure 39: Derived COHO from the PFSS-SCS model for the re-meshed CR2077 magnetogram. The parameters are $R_s = 3.5R_0$, $N = 120$, $N_s = 10$, $N_\phi = 360$, and (a) $N_\theta = 181$, $\Delta\theta = \Delta\phi = 2.5^\circ$, $\Delta r = 0.02R_0$, (b) $N_\theta = 283$, $\Delta\theta = \Delta\phi = 2.5^\circ$, $\Delta r = 0.01R_0$, (c) $N_\theta = 283$, $\Delta\theta = \Delta\phi = 1^\circ$, $\Delta r = 0.01R_0$. $1/F_s$ is saturated at ± 0.1 . The black lines represent open magnetic field lines which connect the sub-Earth positions with COHO.

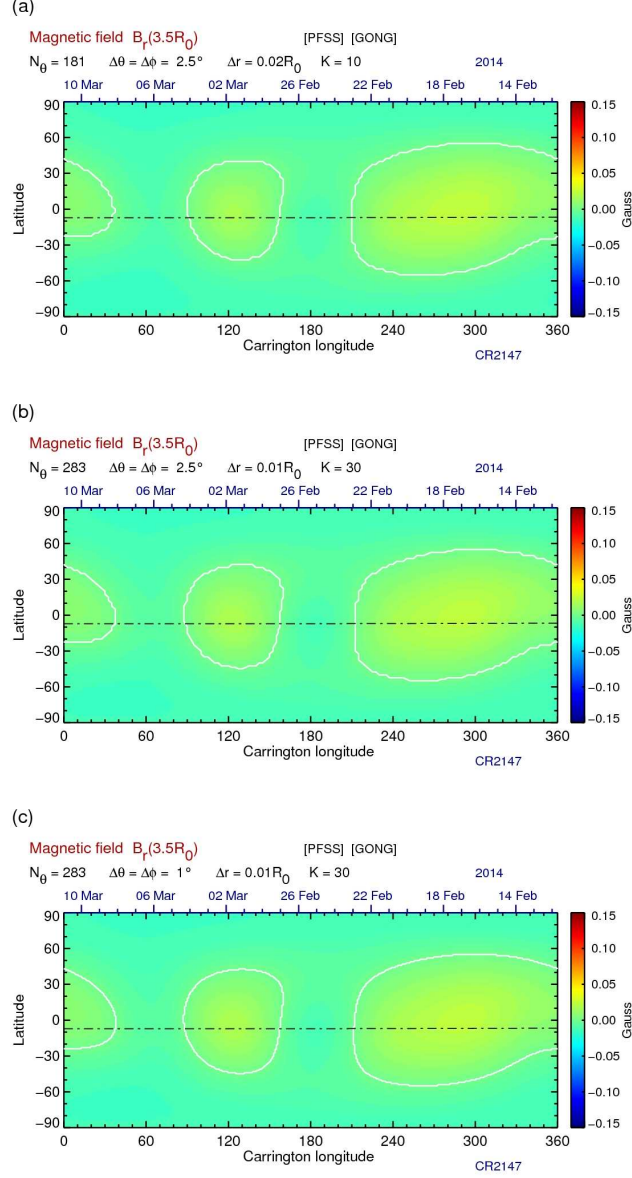


Figure 40: Magnetic field at the source-surface $B_r(1.5R_0, \theta, \phi)$ from the PFSS model for the re-meshed CR2147 magnetogram. The parameters are $R_s = 3.5R_0$, $N = 120$, $N_s = 10$, $N_\phi = 360$, and (a) $N_\theta = 181$, $\Delta\theta = \Delta\phi = 2.5^\circ$, $\Delta r = 0.02R_0$, (b) $N_\theta = 283$, $\Delta\theta = \Delta\phi = 2.5^\circ$, $\Delta r = 0.01R_0$, (c) $N_\theta = 283$, $\Delta\theta = \Delta\phi = 1^\circ$, $\Delta r = 0.01R_0$. The field is saturated at ± 0.15 G. White line represents the neutral line and dash-dot line denotes the sub-Earth positions.

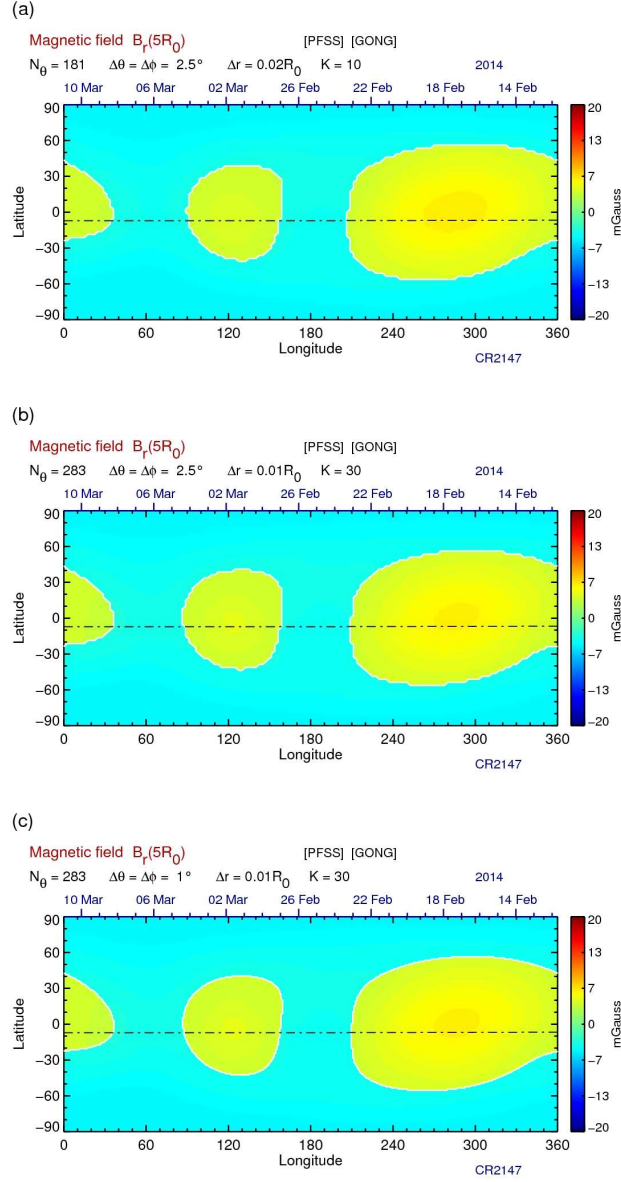


Figure 41: Magnetic field $B_r(5R_0, \theta, \phi)$ from the SCS model for the re-meshed CR2147 magnetogram. The parameters are $R_s = 3.5R_0$, $N = 120$, $N_s = 10$, $N_\phi = 360$, and (a) $N_\theta = 181$, $\Delta\theta = \Delta\phi = 2.5^\circ$, $\Delta r = 0.02R_0$, (b) $N_\theta = 283$, $\Delta\theta = \Delta\phi = 2.5^\circ$, $\Delta r = 0.01R_0$, (c) $N_\theta = 283$, $\Delta\theta = \Delta\phi = 1^\circ$, $\Delta r = 0.01R_0$. The field is saturated at ± 0.2 mG. White line represents the neutral line and dash-dot line denotes the sub-Earth positions.

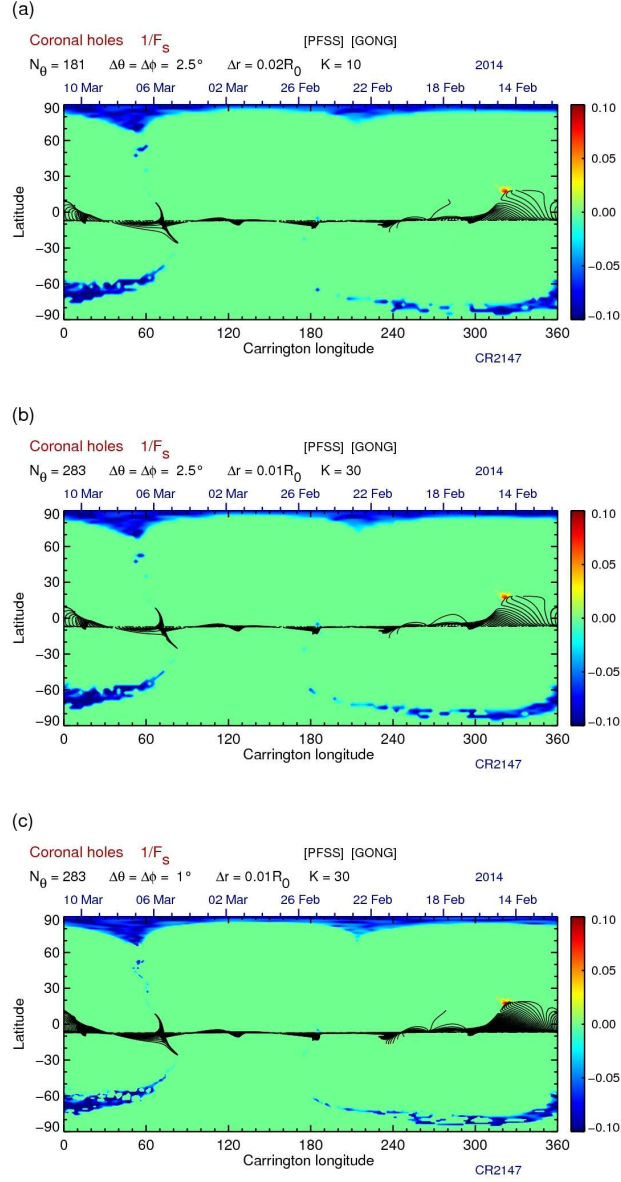


Figure 42: Derived COHO from the PFSS-SCS model for the re-meshed CR2147 magnetogram. The parameters are $R_s = 3.5R_0$, $N = 120$, $N_s = 10$, $N_\phi = 360$, and (a) $N_\theta = 181$, $\Delta\theta = \Delta\phi = 2.5^\circ$, $\Delta r = 0.02R_0$, (b) $N_\theta = 283$, $\Delta\theta = \Delta\phi = 2.5^\circ$, $\Delta r = 0.01R_0$, (c) $N_\theta = 283$, $\Delta\theta = \Delta\phi = 1^\circ$, $\Delta r = 0.01R_0$. $1/F_s$ is saturated at ± 0.1 . The black lines represent open magnetic field lines which connect the sub-Earth positions with COHO.

5 Summary

The Sun’s magnetic field is a key component that influences solar phenomena which are the source of space weather. To derive the global coronal magnetic field, based on observations of the magnetic field at the photosphere, different approaches are used. In this paper, the so-called potential-field source-surface (PFSS) and Schatten current sheet (SCS) approaches were described [9]-[12]. Both models utilize potential-field theory and solutions in the form of spherical harmonics to obtain the field. While the PFSS derived field is based on the current-free assumption in the region $R_0 \leq r \leq R_s$, the SCS solution for the field in the region $r \geq R_{cp}$ implies the existence of thin current-sheets between magnetic field structures of opposite polarity.

Although the PFSS and SCS models represent relatively simple approaches to the problem of mapping the coronal magnetic field, they are widely used. In particular, in operational applications they can be used to forecast magnetic polarity and solar wind speed at the Earth (see e.g. [13]-[17]). For example, the WSA model [13], [14], uses the PFSS-SCS model to derive open magnetic field lines and their flux tube expansion factors f_s Eq. (70). In the WSA model, the angular separation between the open magnetic field line footpoint and the coronal hole boundary θ_b at the photosphere is also calculated. f_s and θ_b are then correlated with the solar wind speed V_{sw} using

$$V_{sw} \left[\frac{\text{km}}{\text{s}} \right] = a_1 + \frac{a_2}{(1 + f_s)^{a_3}} \left[a_4 - a_5 \exp \left\{ - \left(\frac{\theta_b}{a_6} \right)^{a_7} \right\} \right]^{a_8}, \quad (79)$$

where a_1 - a_8 are empirical numerical coefficients [15].

A numerical code for the global coronal magnetic field based on the coupled PFSS and SCS models has been developed. The results in this paper show advantages of the magnetogram re-meshing, and justifies the choices of numerical parameters used in the model. We plan to use the developed code as part of the CSWFC solar wind forecast framework.

To illustrate the capability of the developed code to reproduce observed coronal features, Fig. 43 compares observed COHO obtained by the SDO satellite on 31 December 2013 (17:15UT) [3], and the derived COHO obtained using the developed CSWFC PFSS-SCS code. The GONG magnetogram (31 December 2013, 17:04UT) is re-meshed with $N_\theta = 181$, the source-surface is set to $R_s = 2.5R_0$, the maximum degree of the harmonics is $N = 120$, $N_s = 20$, the angular and radial resolutions are $\Delta\theta = \Delta\phi = 2.5^\circ$ and $\Delta r = 0.02R_0$, respectively. The colour of the derived COHO is associated with the polarity of the magnetic field lines. The lines are directed away from (red colour) and toward (blue colour) the surface of the Sun. The black lines represent open magnetic field lines which connect the sub-Earth positions with COHO. There is a reasonable agreement between the location of the observed and numerically modelled COHO. This gives confidence that the developed code is providing useful models of COHO that can be used in operational space weather forecasting.

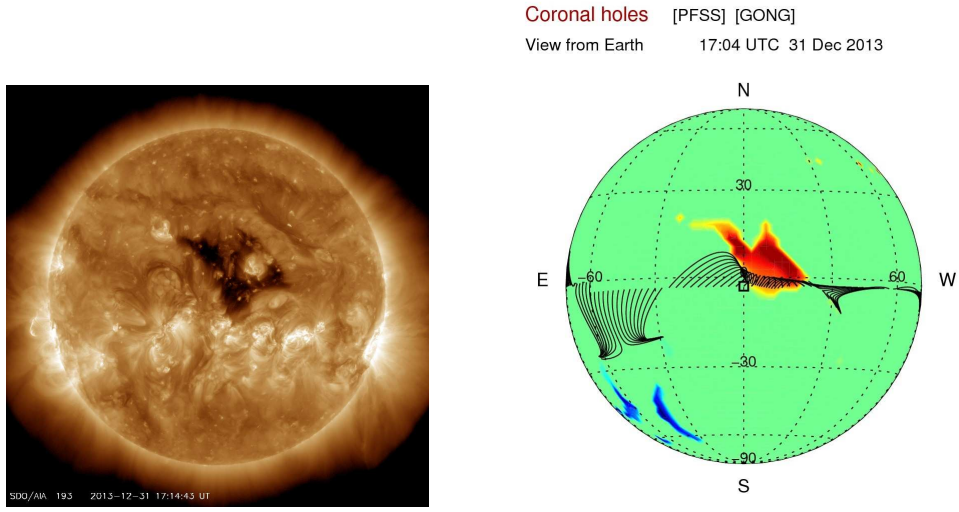


Figure 43: SDO satellite AIA-193 image of the Sun on 31 December 2013 (17:15UT), and derived COHO using the PFSS-SCS model. The parameters used in the model are $R_s = 2.5R_0$, $N = 120$, $N_s = 20$, $N_\theta = 181$, $N_\phi = 360$, $\Delta\theta = \Delta\phi = 2.5^\circ$, and $\Delta r = 0.02R_0$. An hourly updated GONG magnetogram is used as the input to the model. The red and blue colours represent the magnetic field line polarity, i.e. the lines are directed away from and toward the surface of the Sun, respectively. The black lines represent open magnetic field lines which connect the sub-Earth positions with the photosphere.

Acknowledgment

This work utilizes data obtained by the Global Oscillation Network Group (GONG) Program, managed by the National Solar Observatory, which is operated by AURA, Inc. under a cooperative agreement with the National Science Foundation. The data were acquired by instruments operated by the Big Bear Solar Observatory, High Altitude Observatory, Learmonth Solar Observatory, Udaipur Solar Observatory, Instituto de Astrofísica de Canarias, and Cerro Tololo Interamerican Observatory. This work was performed as part of Natural Resources Canada's Public Safety Geoscience program. The author would like to thank Dr R. Fiori, Dr D. Boteler, and Dr L. Trichtchenko, Natural Resources Canada, for reviewing this paper.

References

- [1] International Space Environment Service.
<http://www.spaceweather.org>
- [2] Space Weather Canada.
<http://www.spaceweather.ca>
- [3] Solar Dynamics Observatory.
<http://sdo.gsfc.nasa.gov>
- [4] S. R. Cranmer, Coronal holes, *Living Rev. Solar Phys.* **6**, 3 (2009).
- [5] K. F. Tapping, The 10.7 cm solar radio flux (F10.7), *Space Weather* **11**, 394 (2013).
- [6] National Solar Observatory, Global Oscillation Network Group.
<http://gong.nso.edu>
- [7] D. H. Mackay and A. R. Yates, The Sun's global photospheric and coronal magnetic fields: Observations and models, *Living Rev. Solar Phys.* **9**, 6 (2012).
- [8] P. Riley *et al.*, A comparison between global magnetohydrodynamic and potential field source surface model results, *Astrophys. J.* **653**, 1510 (2006).
- [9] M. D. Altschuler and G. Newkirk, Magnetic field and the structure of the solar corona, *Sol. Phys.* **9**, 131 (1969).
- [10] K. H. Schatten, J. M. Wilcox, and N. F. Ness, A model of interplanetary and coronal magnetic fields, *Sol. Phys.* **6**, 442 (1969).
- [11] M. D. Altschuler *et al.*, High resolution mapping of the magnetic field of the solar corona, *Sol. Phys.* **51**, 345 (1977).
- [12] K. H. Schatten, Current sheet magnetic model for the solar corona, *Cosmic Electrodynamics* **2**, 232 (1971).
- [13] C. N. Arge and V. J. Pizzo, Improvement in the prediction of solar wind conditions using near-real time solar magnetic field updates, *J. Geophys. Res.* **105**, 465 (2000).
- [14] C. N. Arge *et al.*, Improved method for specifying solar wind speed near the Sun, *Solar Wind Ten*, Conference Proceedings, vol. 679, p. 190, 2003.
- [15] P. MacNeice, Validation of community models: 2. Development of a baseline using Wang-Sheeley-Arge model, *Space Weather* **7**, S12002 (2009).
- [16] K. Hakamada *et al.*, Solar wind speed and expansion rate of the coronal magnetic field in solar maximum and minimum phases, *Sol. Phys.* **207**, 173 (2002).
- [17] D. C. Norquist and W. C. Meeks, A comparative verification of forecasts from two operational solar wind models, *Space Weather* **8**, S12005 (2010).
- [18] O. Cohen *et al.*, Validation of a synoptic solar wind model, *J. Geophys. Res.* **113**, A03104 (2008).

- [19] P. MacNeice, B. Elliott, and A. Acebal, Validation of community models: 3. Tracing field lines in heliospheric models, *Space Weather* **9**, S10003 (2011).
- [20] V. J. Pizzo *et al.*, Wang-Sheeley-Arge-Enlil cone model transitions to operations, *Space Weather* **9**, S03004 (2011).
- [21] G. A. Gary, Plasma beta above a solar active region: Rethinking the paradigm, *Solar Phys.* **203**, 71 (2001).
- [22] T. Wiegmann, Solar force-free magnetic fields, *Living Rev. Solar Phys.* **9**, 5 (2012).
- [23] G. Cain and G. H. Meyer, Separation of variables for partial differential equations: An eigenfunction approach studies in advanced mathematics, Chapman & Hall/CRC, 2006.
- [24] S. Chapman and J. Bartels, *Geomagnetism Vol. 2*, Oxford University Press, 1940.
- [25] D. E. Winch *et al.*, Geomagnetism and Schmidt quasi-normalization, *Geophys. J. Int.* **160**, 487 (2005).
- [26] Y.-M. Wang and N. R. Sheeley, Solar implications of ULYSSES interplanetary field measurements, *Astrophys. J.* **447**, L143 (1995).
- [27] S. L. McGregor *et al.*, Analysis of the magnetic field discontinuity at the potential field source surface and Schatten current sheet interface in the Wang-Sheeley-Arge model, *J. Geophys. Res.* **113**, A08112 (2008).
- [28] X. Zhao and J. T. Hoeksema, A coronal magnetic field and plasma model with horizontal volume and sheet currents, *Sol. Phys.* **151**, 91 (1994).
- [29] X. Zhao and J. T. Hoeksema, Prediction of the interplanetary magnetic field strength, *J. Geophys. Res.* **100**, 19 (1995).
- [30] NASA. CFITSIO - A FITS file subroutine library.
<http://heasarc.gsfc.nasa.gov/fitsio/>
- [31] G. Tóth *et al.*, Obtaining potential field solution with spherical harmonics and finite differences, *Astrophys. J.* **732**, 102 (2011).
- [32] J. Meeus, *Astronomical formulae for calculators*, 1979.
- [33] D. Potts, G. Steidl, and M. Tasche, Fast and stable algorithms for discrete spherical Fourier transforms, *Linear Algebr. Appl.* **275**, 433 (1998).
- [34] R. Suda and M. Takami, A fast spherical harmonics transform algorithm, *Math. Comput.* **71**, 703 (2001).
- [35] C. O. Lee *et al.*, Coronal field opens at lower height during the solar cycles 22 and 23 minimum periods: IMF comparison suggests the source surface should be lowered, *Sol. Phys.* **269**, 367 (2011).
- [36] W. M. Arden *et al.*, A “breathing” source-surface for cycles 23 and 24, *J. Geophys. Res.* **119**, 1476 (2013).